Large Eddy and mixed-layer model simulations of the Stratocumulus to Cumulus transition as observed during ASTEX

J.J. van der Dussen

Master's thesis

Supervisor:
Dr. S.R. de Roode

Clouds, Climate and Air Quality
Department of Multi-Scale Physics
Faculty of Applied Sciences
Delft University of Technology

September 4, 2009

"He draws up the drops of water,
which distill from the mist as rain;
the clouds pour down their moisture
and abundant showers fall on mankind."

Job 36:27–28; NIV Study Bible

Cover page: 3D plot of the instantaneous liquid water content as diagnosed by DALES after 8 hours (left) and after 40 hours (right) of simulated time. Dark spots have high liquid water content, while white, partly transparent parts have a low liquid water content. The domain size is $6.4 \times 6.4 \times 2.5$ km^3 with 128^3 gridboxes, resulting in a resolution of 50 m in the $x-$ and $y-$direction and 20 m in the $z-$direction.

Abstract

A basic introduction on stratocumulus clouds and the problems climate and weather forcasting models have in modeling them is given. The governing equations for atmospheric (thermo)dynamics are presented, leading to the filtered equations that are numerically solved in the Dutch Atmospheric Large-Eddy Simulation (DALES) model. The governing equations of the Mixed-Layer Model, a simpler, single slab model, are also presented and discussed. Both models are used to simulate a stratocumulus topped boundary layer using two model intercomparison cases, that are based on data gathered during the Atlantic Stratocumulus Transition Experiment (ASTEX).
Since the code of DALES has been modified significantly during the last decade, the results of these intercomparison cases are also compared to the results obtained, using an older model version (Cuijpers and Duynkerke, 1993). It is shown that the entrainment rate, as diagnosed by the most recent model, is much lower than that in the model of Cuijpers, which is desirable since the latter was incapable of correctly simulating the stratocumulus topped boundary layer as was observed during DYCOMS II (Stevens et al., 2005).
A new intercomparison case based on the entire transition from stratocumulus to cumulus clouds as observed during the first Lagrangian of ASTEX is also presented. The mean boundary layer state, as well as the increase in time of the buoyancy flux in the Large-Eddy Simulation results, compare very well to the data gathered during the experiment. Larger differences are found in the surface fluxes of heat and moisture, likely causing the inconsistency between the measured and simulated profiles of the vertical velocity variance, during the first 8 hours of the simulation. The appearance of cumuli penetrating the thinning stratocumulus layer, a frequently observed process in stratocumulus air masses that are advected equatorwards, is also observed in the Large-Eddy Simulation results.
A Mixed-Layer Model, in which the entrainment rate, the surface fluxes of heat and moisture and the precipitation rate are prescribed from the results of DALES, is used to evaluate how well-mixed the boundary layer is, in the simulation of the transition. During the first 16 hours, the results of both models agree very well. In the remainder of the simulation, the model results of DALES and the Mixed-Layer Model diverge, due to decoupling of the boundary layer.
Finally, a Mixed-Layer Model, in which entrainment, surface fluxes and precipitation are parametrized, is also used to simulate the transition. This model shows large differences with the Large-Eddy Simulation results, mainly caused by the bad representation of the effect of solar radiation on the entrainment rate. Parametrized entrainment rates are severely underestimated during daytime, resulting in large differences in boundary layer height between Large-Eddy Simulation and Mixed-Layer Model results.

Contents

1 Introduction **1**
1.1 Background . . . 1
1.2 Basics of stratocumulus clouds . . . 2
1.3 Decoupling and transition to cumulus . . . 5
1.4 Measurements . . . 6
1.5 Outline . . . 7

2 Modeling **9**
2.1 Thermodynamics . . . 9
2.1.1 Temperature and humidity . . . 9
2.1.2 Virtual potential temperature flux . . . 13
2.2 Governing equations . . . 14
2.2.1 Conservation of mass . . . 14
2.2.2 Conservation of momentum . . . 14
2.2.3 Conserved variable equations . . . 15
2.3 Dutch Atmospheric Large Eddy Model . . . 15
2.3.1 Filtered equations . . . 16
2.3.2 Closure . . . 18
2.3.3 Source/sink terms . . . 20
2.4 Mixed layer model . . . 22
2.4.1 Model equations . . . 22
2.4.2 Entrainment . . . 24
2.4.3 Source/sink terms . . . 27
2.4.4 Turbulent fluxes at night, without precipitation . . . 28

3 Atlantic Stratocumulus Transition Experiment **31**
3.1 ASTEX Observations . . . 31
3.2 Setup of model intercomparison cases . . . 33
3.2.1 Intercomparison based on flight A209 . . . 33
3.2.2 Intercomparison based on flight RF06 . . . 34
3.2.3 New intercomparison based on entire transition . . . 35

4 Results model intercomparison cases **39**
4.1 Model intercomparison based on flight A209 . . . 39
4.2 Model intercomparison based on flight RF06 . . . 42
4.3 Influence of precipitation . . . 44

5 LES and MLM results of the ASTEX Sc to Cu transition **49**
5.1 Mean state 49
5.2 Turbulence structure of the BL 52
5.3 Comparison of MLM to LES results of the transition 55
5.3.1 MLM with prescribed entrainment, surface flux and precipitation . 56
5.3.2 MLM independent of LES results 56

6 Conclusions and outlook **61**
6.1 Conclusions 61
6.1.1 Model intercomparison 61
6.1.2 Transition as simulation by DALES 61
6.1.3 Mixed-Layer Modeling of the transition 62
6.2 Outlook 62
6.2.1 Analysis using DALES 62
6.2.2 Possibilities of the MLM 63

A List of symbols and abbreviations **69**

Chapter 1

Introduction

1.1 Background

In recent years weather and world climate have been the subject of much scientific and political debate. Accurate weather prediction is becoming more and more important, as rain or snow can result in dangerous situations and traffic jams, that have a strong influence on everyday life. Furthermore, climate change is a worldwide problem. The measured increase in global mean temperature, caused by or at least influenced by human activity, is a point of concern for many people all over the world. Much research has already been done in this field on widely varying topics such as the change in sea level, global food production, increased risks of flooding, the dangers for biodiversity etc. In atmospheric research areas, climate change is of particular interest. Climate models attempt to grasp the overall trends in temperature and the effect of human activity over periods of up to 100 years. Weather forecasting models, on the other hand, have far shorter time and length scales, making it possible to do more accurate predictions concerning the upcoming weather in a certain area.
There are however large uncertainties in both kinds of models, that influence the reliability of the predictions made. Clouds are among the largest of these uncertainties (Houghton et al., 1997). The gridsize (the smallest scale that can be resolved) is usually much larger than the turbulent eddies that are important for the formation of clouds, even for weather forecasting models. Therefore they have to be parametrized. The parametrizations used are far from perfect, which makes It is not yet entirely clear what impact this has on longterm predictions. One of the major questions are for instance: How will the amount of clouds change with changing climate? The research presented in this report should be viewed in the light of these questions.

The main topic of interest in this thesis is the stratocumulus cloud type. One might wonder: of all the cloud types, why focus on this one? This is because of the large influence these clouds have in general (Figure 1.1). Together with cumulus and stratus, stratocumulus clouds constitute the low-level clouds, which are characterized by their low altitude of two kilometers or less. Low-level clouds are the most abundant form of clouds, judging from the yellow-orange area in Figure 1.1(b). A peak in occurrence lies somewhere in between the cumulus and stratocumulus regime. However, due to the much higher cloud cover of stratocumulus clouds, their area averaged optical thickness is much higher. Therefore, the overall impact of stratocumulus on the global energy

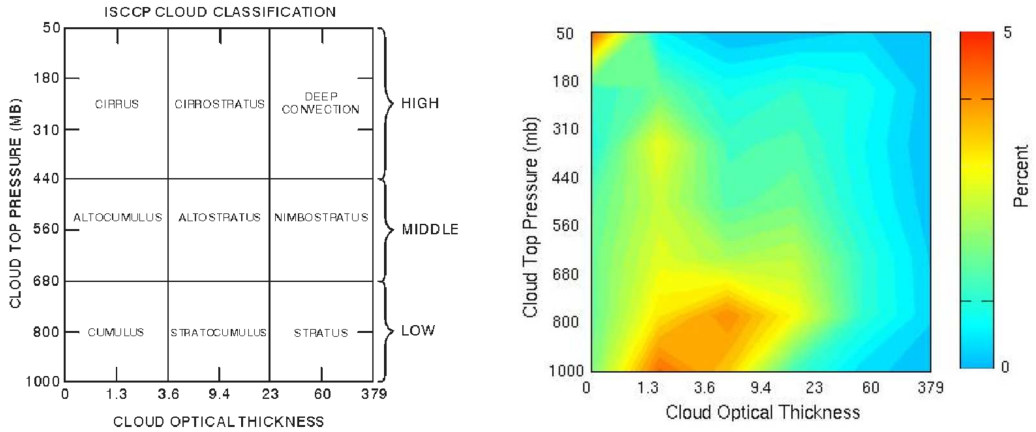

(a) (b)

Figure 1.1: Cloud classification according to the International Satellite Cloud Climatology Project (ISCCP) as a function of cloud top pressure (height) and cloud optical thickness (Rossow and Schiffer, 1999) (a). Information gather by satellites over the period of 1983-2008, has led to the diagram shown the right, which shows the globally averaged occurrence of each combination of optical thickness and cloud top height (b).

balance is higher than that of cumulus clouds.
The strong dependence of low-level clouds on the local turbulent structure of the BL, makes their parametrization particularly difficult. Large Eddy Simulation (LES) models typically use grid sizes of the order of tens of meters, which allows them to solve much of the turbulence. In theory, LES can be used instead of parametrization in a weather forecasting model. In practice however, running such a model, is computationally much to expensive. It would require days to make a decent weather forecast.
Still, a LES model is an ideal tool for scientific purposes. It can help to gain insight into the processes that are important for the lifecycle of low-level clouds. The high resolution limits subgrid parametrization to a minimum, making LES ideal for meteorologists to try to improve the parametrizations that are currently used in large scale models. Only recently, computers became powerful enough to make long simulations on a domain of a few km^3 possible and therefore, LES simulations and models receive much attention.

1.2 Basics of stratocumulus clouds

As mentioned before, stratocumuli belong to the class of low-level clouds. These clouds are, due to their low altitude, heavily influenced by the conditions at the earth's surface. A continuous supply of moisture is a prerequisite for the clouds not to dissolve. Therefore, stratocumulus (Sc) is most frequently observed over seas. Over land it usually does not persist due to lack of moisture and an increased rate of heating. Figure 1.2 is a good example of this. A relatively small patch of Sc covers a large part of the North Sea, however, above land (Great Britain and The Netherlands) skies are virtually cloudless. Above the IJsselmeer and the water-rich province of Zeeland patches of Sc can also be seen, showing the large influence of the surface even better. This is the reason that in this thesis, only marine Sc is considered. Cooler ocean currents, for instance along the coasts of California and Peru, are ideal conditions for Sc to form and to persist for several days, covering areas of millions of km^2.

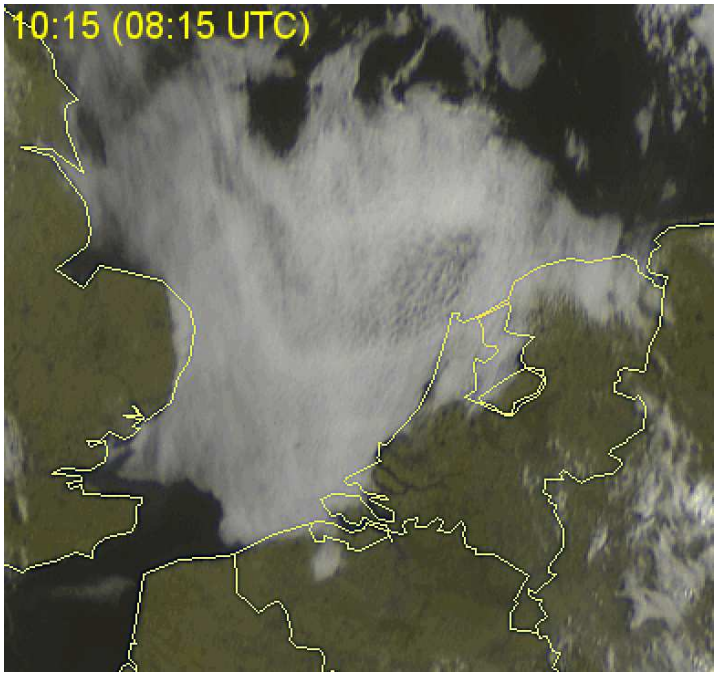

Figure 1.2: A relatively small stratocumulus field over the North Sea, before the coast of The Netherlands, June 30, 2009 at 08:15 UTC. The edges of the cloud follow the coastline of both Great Britain and The Netherlands. The mean wind was from the northeast advecting the Sc field towards the Strait of Dover. The image is made by a EUMETSAT satellite.

Hadley Circulation

The mentioned areas, the coasts of Peru and California, have something else in common: both are located close to the so-called horse latitudes. These are formed by the latitudes between 30 and 35 degrees North and South. What is special about the locations is that the average motion of air is in a downward direction. The reason for this is that the insolation is highest around the equator. Therefore, air rises here and is transported through the atmosphere. Around the horse latitudes the air comes down, causing the typical descending motion. At the surface, mean wind is in the opposite direction towards the equator, forming the trade winds. A schematic view of this circulation, called the Hadley circulation, is found in Figure 1.3.

The air that descends is warm and dry as compared to the air at the surface. Since the denser air lies below the warm, less dense air, a very stable situation is formed. The interface between the two layers is usually called the 'inversion'. The stronger the temperature gradient at the inversion, the more stable the inversion. The air below the inversion constitutes the Atmospheric Boundary Layer (ABL) or just Boundary Layer (BL), while everything above it is called the Free Atmosphere (FA). The inversion acts as a lid on top of the BL: thermals rising from the surface are hardly able to pass it. Therefore, turbulence is confined to the BL and the FA is mostly laminar. It also means that there is hardly any transport of moist from the surface to the FA, it is confined to the BL. This results in a relatively high humidity, allowing a layer of clouds to form at the top of the BL.

As the clouds are advected towards the equator, the subsiding motion of air (subsidence) becomes gradually weaker, while the SST increases. Slowly, the BL deepens and the Sc

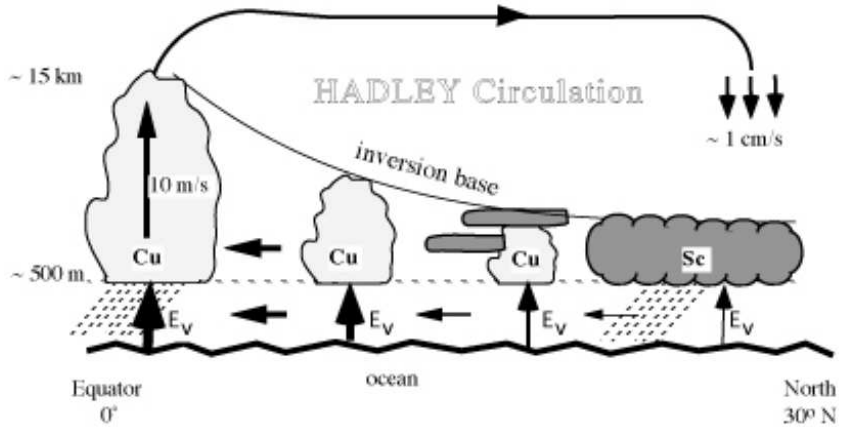

Figure 1.3: A schematic representation of the Hadley circulation. At the equator, evaporation (E_v) is largest, causing air to rise. This air is transported northward (or southward) to about 30° latitude, where the air descends with a velocity of about 1 cm s^{-1} at 1 km height. The sinking relatively warm and dry air causes a stable stratification (inversion) to develop. At the sea surface, winds are in the opposite direction towards the equator. In the process, advected stratocumulus (Sc) dissolves and cumulus clouds (Cu) form (Cuijpers, 1994).

layer dissolves, while Cu clouds form. This transition from Sc to Cu is the main topic of this thesis.

Dynamics and radiation

The processes that control the state of the BL over seas are somewhat different from those over land. During the day, land is easily heated by the sun. This creates a relatively large temperature difference between the surface and the air. Strong thermals rise from the surface, creating turbulence inside the BL. At night, the surface cools again, the thermals become weaker and weaker and the turbulence is much less than during the day. Therefore, a strong diurnal cycle is found over land.
The sea surface is very different from land. Due to the large heat capacity of water and the depth of the water, the influence of absorbed sunlight on the SST is small. This means that the air above the sea has enough time to adjust to the SST. Thermals rising from the surface are therfore not very strong. In Stratocumulus-Topped Boundary Layers (STBLs) another process dominates turbulence generation.
All objects radiate energy with an average wavelength that is proportional to its temperature. Clouds do also. From a certain thickness, Sc clouds even act as pure blackbody radiators. As all cloud droplets radiate and absorb, the net energy due to radiation is zero inside the cloud. At the edges of the cloud, this is not the case. At cloud base, radiation emitted from the surface is absorbed while the cloud itself emits radiation. Due to the higher temperature of the Earth, the former is larger and a slight warming at cloud bottom is observed. At cloud top, however, more radiation is emitted than absorbed, causing a strong negative tendency in temperature. The radiation emitted by the cloud is in the infrared regime, therefore the process is usually referred to as cloud-top longwave radiative cooling. Air parcels at cloud top cool and start to sink, creating downdrafts. These downdrafts create turbulence, hence Sc dynamics are said to be top-driven instead of surface driven.
During the day, longwave radiative cooling is partially or entirely compensated by solar,

or shortwave, radiative warming in the cloud layer. Although most of this shortwave radiation is reflected at cloud top, some is absorbed in the cloud layer, causing a positive tendency in the temperature. The remaining radiation reaches the surface. The absorption takes place throughout the entire cloud layer, but is strongest at the top. Air at the top therefore cools less at daytime than during the night. Cold downdrafts are less severe and therefore, less turbulence is generated at night (Bennetts et al., 1986).
The radiative properties described influence the temperature of the layer below the cloud significantly. The reflection of a large part of the sunlight, up to 80%, causes less energy to reach this layer, making cloudy days cooler. At night, it is the other way around. Clear nights are generally cooler, because of the energy loss of the surface due to longwave radiation, while during a cloudy night this loss is almost fully compensated by the radiation emitted at cloud bottom. Thus, at night Sc acts as a blanket. For the same reasons, the amount of Sc is important for the total energy balance of the Earth. In this thesis however, the focus is on the effects of radiation on turbulence generation, as described above.
What exactly is the effect of turbulence inside a STBL? On the one hand, turbulence, formed by eddies, mixes the BL. This enables moisture from the surface to reach the upper part of the BL, thickening the cloud. On the other hand, eddies close to the inversion sometimes overshoot it and when they fall back, some of the FA air is dragged with it, into the BL. This process is called entrainment. The stronger the turbulence, the higher the entrainment rate. In light of the discussion above, it is expected that the entrainment rate is highest at night, when longwave cooling dominates the dynamics.
Entrainment is an important process for STBLs. While subsidence pushes down onto the BL, entrainment makes the BL height increase by pulling in air from above the FA. This air is warmer and dryer and therefore the BL slowly warms and dries out.

1.3 Decoupling and transition to cumulus

Many earlier studies focus on entrainment as the main mechanism that causes the breakup of a Sc deck. It was hypothesized that under some conditions, the entrained air causes a decrease in temperature at cloud top, while naively an *increase* is expected due to the higher temperature of the FA air. However, the FA is also dryer, resulting in evaporation of the liquid water in the cloud around the entrained parcel of air. Conditions can be found under which the cooling effect of this evaporation is larger than the warming due to the higher temperature of the air. Under these conditions, the entrained parcel starts to sink, creating an unstable situation at cloud top which increases entrainment in turn. This feedback mechanism, initially proposed by Lilly (1968), was assumed to be the main cause for the rapid dissolving of Sc layers and it is referred to as Cloud Top Entrainment Instability (CTEI).
Many criteria have been constructed to get a grip on this process, but none of these seem to be very accurate. Persisting layers of Sc have been reported at moments that these criteria were met (Albrecht and Penc, 1985; Kuo and Schubert, 1988; Stevens et al., 2003a). Therefore, CTEI is more and more depreciated lately.
Another mechanism was proposed already by Nicholls (1984). He argued that over time, a temperature jump can form in a STBL just below cloud base, caused by solar irradiation, precipitation, the deepening of the BL or a combination of these processes. The stratification has the same effect, albeit weaker, as the inversion: the cloud layer

and the layer below (subcloud layer) become more or less separated from each other, a process called decoupling. The cloud layer is cut-off from moisture coming from the surface, while entrainment keeps drying it out. Slowly but steadily, the liquid water inside the cloud will evaporate, thinning the cloud.
At the same time, moisture builds up in the layer below the stratification due to the evaporation of water at the surface. Some of the stronger thermals can then penetrate the stratification into the layer above, where some of the moisture readily condensates. The heat released in this process causes air in the thermal to rise even faster. The thermals with the most moisture can even penetrate into the Sc at the top of the BL. At this moment, the layers are said to be 'recoupled'. The phenomenon of Cu clouds rising into overlaying thin Sc clouds has been frequently observed.
This last stage of recouping is a large advantage of decoupling over CTEI. It provides in a mechanism that explains the frequently observed transition of Sc to Cu in a very elegant way, while CTEI only predicts the dissolvement of the Sc layer.

1.4 Measurements

Measurements are always an indispensable part of research. This is not any different in meteorological science. There are lots of different parameters that are of influence in BL development, which vary in space and in time. Therefore, doing measurements in a consistent and meaningful way is not an easy task. It requires using many different instruments, a suitable location and much planning. Several large measurement campaigns concerning Sc have been performed, one of the first being FIRE (First ISCCP Regional Experiment). Measurement were taken by means of aircraft flights, probes hanging from balloons and remote sensing by ground stations. Furthermore, satellites produced large scale information of the measurement area (Albrecht et al., 1988). Objects of this campaign were: getting more insight in the interaction of the different physical processes, their effect on the life cycle of Sc and the measurement of the cloud radiative properties. The cloud conditions were ideal: a solid, shallow Sc layer was present for the entire duration of the experiment. The flights took place some 95 kilometers from the west coast of the US.
Later, other field experiments attempted to do measurements with the goal of providing suitable data sets for modelers. The Dynamics and Chemistry of Marine Stratocumulus (DYCOMS) experiments focus on finding the entrainment rate and understanding the microphysical details in stratocumulus clouds (see Stevens et al., 2003b).
FIRE II (First ISCCP Regional Experiment II) differed from these campaigns in the emphasis of the research, which was not on persisting Sc layers, but on the transition of Sc to Cu. It was called the Atlantic Stratocumulus Transition EXperiment (ASTEX) and it concentrates on the evolution of the cloud layer and the vertical structure of Sc as it moves over a sea surface with increasing temperature (Albrecht et al., 1995). The measurements span a period of approximately two days starting from an irregular STBL which evolves during nighttime into a more homogeneous Sc layer. During the day, Cu clouds start to penetrate the cloud deck and it breaks up.

1.5 Outline

In this thesis decoupling of the Sc layer during the ASTEX transition is examined. The emphasis will not be on the presentation of the data gathered during the experiments, but on the reconstruction of the transition starting from flight 2 using the Dutch Atmospheric Large Eddy Simulation (DALES) model. To this end, first of all, some relevant thermodynamics and variables are introduced in chapter 2, which are useful in the subsequent derivations of the governing equations inside the BL. These equations form the basis for the discussion of the model equations of both DALES and a Mixed-Layer Model (MLM).
The following chapter contains information on ASTEX: some measurement details are given, followed by a detailed description of the model intercomparison cases based on the experiment.
Results of these intercomparison cases can be found in chapters 4 and 5. The thesis ends with the presentation of the conclusions, followed by recommendations for research continuing on this, with an emphasis on the MLM.

Chapter 2

Modeling

In this chapter, the governing equations will be presented that are used to describe the ABL. These equations are usually written using variables the reader might not be familiar with. Understanding why these variables are used and what they embody is crucial to the apprehension of the equations. Also, in atmospheric sciences, variables tend to have one or more subscripts, making the equations even less transparent.
Therefore, this chapter starts with the introduction of some useful atmospheric variables. The meaning of these variables and their units can also be found in the list of symbols, located in the back of this thesis. The remainder of this chapter contains the description of the used models, starting with the Dutch Atmospheric Large Eddy Simulation (DALES) model. This LES model contains many thousands of lines of code and it goes beyond the scope of this thesis to discuss it entirely. The model was mostly used as a tool, not as an object of research on itself.
In contrast, the idea behind the Mixed Layer Model (MLM) is simple and the main modeling equations can compactly be written down. The model is written specially for this project, thus the discussion of that model is more extensive and contains most of the equations used.

2.1 Thermodynamics

2.1.1 Temperature and humidity

It is generally known among climbers that at the top of a mountain, air is rarefied, making breathing harder. The cause of this is the gravitational force, pulling molecules towards the Earth. Pressure and density of air are therefore a function of height, an effect described by the hydrostatic balance:

$$\frac{\partial p}{\partial z} + \rho g = 0, \tag{2.1}$$

where p is the pressure, z the height, ρ the density of air and g is the gravitational acceleration. This equations describes a pressure that decreases with height.
When the height of a parcel of air in the atmosphere changes for some reason, it is effected by the change in pressure. In the following discussion, it will be shown that the temperature of the air changes. Mean temperature will therefore also be a function of height. Here, a new temperature (or heat) variable will be introduced, which is not a function of height making it a more convenient variable to work with.

To this end, the first law of thermodynamics (energy conservation) is written in an incremental form:

$$\mathrm{d}h = T\mathrm{d}s + \frac{\mathrm{d}p}{\rho}. \tag{2.2}$$

In this equation, h and s denote the specific enthalpy and entropy respectively, while T is the temperature. A 'd' in front of a variable denotes the change of that variable during the process. In the case of an isentropic process, $\mathrm{d}s = 0$. Furthermore, the enthalpy can be written in terms of temperature, using the specific heat at constant pressure c_p: $\mathrm{d}h = c_p\ \mathrm{d}T$. The result is:

$$c_p \mathrm{d}T = \frac{\mathrm{d}p}{\rho}. \tag{2.3}$$

Under the assumption that air behaves like an ideal gas, which is valid since pressure never exceeds roughly 1050 hPa and temperatures are moderate in the lower atmosphere[1], ρ is substituted out using the ideal gas law:

$$T = \frac{p}{\rho R_d}, \tag{2.4}$$

where R_d is the specific gas constant for dry air: $R_d = 287.05$ J kg^{-1} K^{-1}. The substitution, after rewriting, results in:

$$\frac{\mathrm{d}T}{T} = \frac{R_d}{c_p}\frac{\mathrm{d}p}{p} \quad \Rightarrow \quad \mathrm{d}\ln T = \frac{R_d}{c_p}\mathrm{d}\ln p \tag{2.5}$$

This equation can be integrated from a reference state (p_0,θ) to a second state with a different pressure p and temperature T. The result is:

$$\theta = \frac{T}{\Pi}, \tag{2.6}$$

where

$$\Pi = \left(\frac{p}{p_0}\right)^{R_d/c_p} \tag{2.7}$$

is the Exner function.

Now in the atmosphere, air is never devoid of water: the total humidity q_t, which is the sum of the water content in the vapor ("v") and the liquid ("l") phases:

$$q_t = q_v + q_l, \tag{2.8}$$

is never zero. Since this thesis is concerned only with low-level clouds in the (sub)tropical regime, the ice content q_i is neglected.
The presence of water has some impact on the average properties of the air. In the first place, the buoyancy of a so-called wet air parcel ($q_t \neq 0$) is different from a dry

[1]The reduced pressure of air in the atmosphere p_R is usually below 0.03, while the reduced temperature T_R is typically around 2 inside the BL. The compressibility factor $Z = p/(\rho RT)$ can be found from a generalized compressibility chart, e.g. in Moran and Shapiro (2002), to be very close to unity.

one: water vapour decreases the average density of air, increasing buoyancy, while the presence of liquid water increases the air's density, thus decreasing buoyancy. The ideal gas law, as written in equation (2.4) is not valid anymore. The specific gas constant for a mixture of gases R_m should be used:

$$T = \frac{p}{\rho R_m}, \tag{2.9}$$

where R_m is a function of the amount of water in the air. It is found more convenient to work only with R_d, so the ideal gas law (or a general equation of state) is left unchanged. The dependence of the water content is shifted to the temperature, giving:

$$T_v = \frac{p}{\rho R_d}, \tag{2.10}$$

where T_v is the virtual potential temperature, defined as: the temperature a dry parcel of air would have if it's pressure and temperature were equal to those of moist air. A formal derivation of T_v can be found in, example given Stull (1993). Here the result is given:

$$T_v = \left(1 + \epsilon_I q_t - \frac{q_l}{\epsilon}\right) T, \tag{2.11}$$

where

$$\epsilon_I = \frac{1}{\epsilon} - 1 = \frac{R_v}{R_d} - 1 \cong 0.608. \tag{2.12}$$

Dividing T_v by the Exner function, equation (2.7), results in the virtual potential temperature θ_v, which is, like θ conserved for isentropic pressure changes:

$$\theta_v = \frac{T_v}{\Pi}. \tag{2.13}$$

The following short derivation will show the vary useful properties of the variables introduced above.
The variables $\varphi \in \{T_v, p, \rho\}$ in equation (2.10) can be splitted into a mean part $\overline{\varphi}$ and a deviation from that mean φ'. After rewriting, this gives:

$$\overline{p} + p' = \left(\overline{\rho}\,\overline{T_v} + \rho'\,\overline{T_v} + \overline{\rho}\,T_v' + \rho' T_v'\right) R_d. \tag{2.14}$$

Neglecting the last term on the rhs and dividing by $\overline{p}$ results in:

$$1 + \frac{p'}{\overline{p}} = \frac{\overline{\rho}\,\overline{T_v} R_d}{\overline{p}} + \frac{\rho'\,\overline{T_v} R_d}{\overline{p}} + \frac{\overline{\rho}\,T_v' R_d}{\overline{p}}. \tag{2.15}$$

In this equation $\frac{p'}{\overline{p}} \ll 1$ and is therefore neglected. Furthermore, the first term on the rhs is equal to one, cancelling the one on the lhs. The final results is:

$$\frac{T_v'}{\overline{T_v}} = -\frac{\rho'}{\overline{\rho}}, \tag{2.16}$$

or, after replacing the average values for reference values and dividing numerator and denominator of the lhs by the Exner function:

$$\frac{\theta_v'}{\theta_0} = -\frac{\rho'}{\rho_0}. \tag{2.17}$$

This result shows that fluctuations in the virtual (potential) temperature play the same role as fluctuations in density: they are an indication of the buoyancy of air. The advantage of heat variables over density is that the former can be easily measured, while weighting air to determine it's density is impossible.

There is another process that has not been addressed yet. When clouds form, water is condensed and in this process, heat is released into the surrounding air, warming it. This means that, although liquid water loading is part of θ_v, this quantity is not conserved under phase changes. To compensate for the evaporation/condensation of water and the energy involved in these processes, yet another variable with units Kelvin is introduced, namely the liquid water potential temperature, θ_l:

$$\theta_l \approx \theta - \frac{L}{c_p} q_l, \tag{2.18}$$

with L the latent heat of evaporation of water. Another frequently used variable with exactly the same purpose is the equivalent potential temperature θ_e:

$$\theta_e \approx \theta + \frac{L}{c_p} q_v = \theta_l + \frac{L}{c_p} q_t. \tag{2.19}$$

A more or less formal derivation of these quantities from conservation of entropy (isentropic processes are assumed) can be found in Betts (1973) and in de Roode (2004).
The pressure together with any two of the variables q_t, θ_l or θ_e defines the thermodynamic state of the entire BL. The choice of which of these to use is arbitrary. For this thesis, the system $\{q_t,\theta_l\}$ is chosen, following Deardorff (1976). The main advantage of θ_l over θ_e is that $\theta_l = \theta$ in the unsaturated case. Since θ (or: T) is the variable of interest, this makes θ_l more insightful. Sometimes, using the liquid water static energy s_l is preferred, which use is equal to that of θ_l:

$$s_l = \theta_l c_p. \tag{2.20}$$

Table 2.1.1 gives an overview of the use of the temperature variables discussed above.

Table 2.1: A summary of temperature variables. Different columns show different condition: a completely dry atmosphere ($q_t = 0$), a wet atmosphere without liquid water ($q_t > 0, q_l = 0$) and a moist atmosphere containing liquid water (clouds) $q_l > 0$. The rows show the different equations for which the temperature variables are appropriate (de Roode, 2004).

	$q_t = 0$	$q_t > 0, q_l = 0$	$q_l > 0$
ideal gas law	T	T_v	T_v
conservation of momentum	θ	θ_v	θ_v
conservation of heat/entropy	θ	θ_v	θ_l or θ_e

A last frequently used quantity in the description of cloudy BLs is the liquid water path (LWP, or for convenience W), which is the vertical integral of q_l:

$$W = \int_0^{z_i} \rho q_l \mathrm{d}z. \tag{2.21}$$

This quantity is useful in calculations concerning, example given the absorption of shortwave radiation of the cloud layer. An advantage of W is that it can directly be estimated by satellite measurements, providing in a crude way of model validation.

2.1.2 Virtual potential temperature flux

As mentioned above, the virtual potential temperature is an important property which is directly linked to buoyancy. Since both DALES and the MLM solve q_t and θ_l, it is useful to derive equations for θ_v in terms of these variables. To arrive at them, first equation (2.11) is divided by the Exner function. Then equation (2.18) can be used to substitute out θ. The result is then:

$$\theta_v = \left(1 + \epsilon_I q_t - \frac{q_l}{\epsilon}\right)\left(\theta_l + \frac{L}{c_p} q_l\right). \tag{2.22}$$

Under the assumption that supersaturation is negligible in STBLs (see e.g. Albrecht et al., 1995, fig. 9), the total humidity can be written as:

$$q_t = q_s + q_l, \tag{2.23}$$

where q_s is the saturation specific humidity. Substitution of this equation in equation (2.22) and using equation (2.73) to split all variables into a Reynolds-averaged part and a fluctuation, gives after proper rewriting:

$$\theta_v' = (\epsilon_I q_s' - q_l')\left(\overline{\theta_l} + \frac{L}{c_p}\overline{q_l}\right) + [1 + \epsilon_I(\overline{q_s} + q_s') - (\overline{q_l} + q_l')]\left(\theta_l' + \frac{L}{c_p} q_l'\right). \tag{2.24}$$

Next, this entire equation is multiplied by the vertical velocity fluctuation w' and the Reynolds-averaging operator is applied, resulting in:

$$\overline{w'\theta_v'} = (\epsilon_I \overline{w'q_s'} - \overline{w'q_l'})\left(\overline{\theta_l} + \frac{L}{c_p}\overline{q_l}\right) + (1 + \epsilon_I \overline{q_s} - \overline{q_l})\left(\overline{w'\theta_l'} + \frac{L}{c_p}\overline{w'q_l'}\right), \tag{2.25}$$

where terms of the form $\overline{w'\varphi_1'\varphi_2'}$ (third order moments) have been neglected.
Below the cloud in a STBL, where air is not saturated, $q_l = 0$ and therefore also $\overline{w'q_l'}$. Furthermore, the substitution $q_s = q_t$ can be used, resulting in:

$$\overline{w'\theta_v'} = A_d\overline{w'\theta_l'} + B_d\overline{w'q_t'} \qquad \text{for } q_t < q_s. \tag{2.26}$$

Here A_d and B_d are coefficients for this unsaturated case:

$$A_d = 1 + \epsilon_I \overline{q_t} \approx 1.01, \tag{2.27}$$

$$B_d = \epsilon_I \overline{\theta_l} \approx 180. \tag{2.28}$$

Air inside the cloud is of course saturated, so the approximation used above is not valid. Still an equation similar to equation (2.26) can be written:

$$\overline{w'\theta_v'} = A_w\overline{w'\theta_l'} + B_w\overline{w'q_t'} \qquad \text{for } q_t > q_s. \tag{2.29}$$

The coefficients are now given by more complex relations:

$$A_w = \frac{1 + \frac{\overline{q_s}}{\epsilon} - \overline{q_t} + \frac{\overline{\theta}}{\epsilon}\frac{\mathrm{d}q_s}{\mathrm{d}T}}{1 + \frac{L}{c_p}\frac{\mathrm{d}q_s}{\mathrm{d}T}} \approx 0.5, \tag{2.30}$$

$$B_w = A_w\frac{L}{c_p} - \overline{\theta} \approx 1000. \tag{2.31}$$

A derivation of these equations, in which fluxes of q_s and q_l are substituted out using the Clausius Clapeyron equation, is given by among others de Roode (2004, pp.52). The equations above will turn out to be very convenient in combination with the MLM.

2.2 Governing equations

The description of the atmosphere starts by determining what the conserved variables are and writing down conservation equations for them. Conserved variables are as always: mass, momentum and energy. Energy conservation is, in light of the discussion of the previous section, written in terms of the liquid water potential energy. An extra conserved variable is the total humidity, q_t.

2.2.1 Conservation of mass

Of these equations, conservation of mass is most easily written down:

$$\frac{\partial \rho}{\partial t} + \frac{\partial \rho u_j}{\partial x_j} = 0. \tag{2.32}$$

In this equation, x_j represents the three cartesian coordinates: $(x_1,x_2,x_3) = (x,y,z)$ and u_j represents the velocity in the x_j direction. Note that the notation implicitly assumes a summation over the index j. It is perhaps more convenient to write this equation in a somewhat different form, which can be done by using standard differentiation rules and the definition of the total derivative. The result is then:

$$\frac{\mathrm{d}\rho}{\mathrm{d}t} + \rho\frac{\partial u_j}{\partial x_j} = 0. \tag{2.33}$$

For shallow boundary layers, incompressibility of air is usually assumed. In this case, the first term of the continuity equation is zero, giving:

$$\frac{\partial u_j}{\partial x_j} = 0. \tag{2.34}$$

2.2.2 Conservation of momentum

Momentum conservation can be used to describe the velocity of the air. It consists of three equations, one for every direction. For fluid and gas flow, the Navier-Stokes equations are used:

$$\rho\left(\frac{\partial u_i}{\partial t} + \frac{\partial u_j u_i}{\partial x_j}\right) = -\frac{\partial p}{\partial x_i} + \frac{\partial}{\partial x_j}\left(\mu\frac{\partial u_i}{\partial x_j}\right) + F_{ijk}, \tag{2.35}$$

where again, the implicit sum is over index j. Furthermore, p is the pressure and F_{ijk} denotes external body forces acting on a parcel. Index $i \in \{1,2,3\}$ denotes the number of the equation.
In the atmosphere, there are only two body forces important. The first is, of course, gravity. The gravitational force is described by: $F_i^g = -\delta_{i3}\rho g$. Here, δ_{ij} is the Kronecker delta, which has the properties:

$$\delta_{ij} = \begin{cases} 0 & \text{for} \quad i \neq j \\ 1 & \text{for} \quad i = j \end{cases}$$

The second force that acts on an atmospheric system is the Coriolis force, caused by the rotation of the earth, represented by:

$$F_{ijk}^c = -2\rho\epsilon_{ijk}\omega\eta_j u_k, \tag{2.36}$$

where ϵ_{ijk} is the alternating unit tensor, which has the properties:

$$\epsilon_{ijk} = \begin{cases} -1 & \text{for} \quad ijk = 321, 132, 213 \\ 0 & \text{for} \quad \text{if any two or more of the indices are equal} \\ +1 & \text{for} \quad ijk = 123, 312, 231 \end{cases}$$

Furthermore, ω is the angular velocity (scalar) of the earth and $\overrightarrow{\eta}$ is a unit vector parallel to the earth's axis of rotation: $\overrightarrow{\eta} = (0, \cos\phi, \sin\phi)$, where ϕ is the latitude. Equation (2.36) is just a way of representing a cross product between the earth's angular velocity and the velocity of the air. Finally, the Navier-Stokes equations become:

$$\rho\left(\frac{\partial u_i}{\partial t} + \frac{\partial u_j u_i}{\partial x_j}\right) = -\frac{\partial p}{\partial x_i} - \delta_{i3}\rho g - 2\rho\epsilon_{ijk}\omega\eta_j u_k, \tag{2.37}$$

in which the effect of viscosity is neglected, since it is orders of magnitude smaller than the other terms.

2.2.3 Conserved variable equations

In the Thermodynamics section, it was already noted that there are several conserved variables and that a combination of any two of them can be used to describe the system. A convenient set of variables is formed by the liquid water potential temperature θ_l together with the total water content q_t. The general conservation equation for these variables is:

$$\frac{\partial \varphi}{\partial t} + \frac{\partial \varphi u_j}{\partial x_j} = S_\varphi, \tag{2.38}$$

where S_φ is a sink/source term of the variable φ to include effects for which it is not conserved. In the case of q_t and θ_l these processes include radiation (longwave cooling and shortwave absorption), freezing/melting and precipitation. Since this thesis is solely concerned with shallow boundary layers, freezing/melting processes are neglected. Both radiation and precipitation (including gravitational settling) are modeled.

2.3 Dutch Atmospheric Large Eddy Model

Analytical solutions to the governing equations are not common in meteorology. Simulation using computer models is therefore required. A virtually exact solution can be provided by a Direct Numerical Simulation (DNS), which solves the equations in the previous section for all length scales involved. In the atmosphere, length scales span the entire range from the smallest (the Kolmogorov length, of the order of a mm) to the very largest (of the order of the boundary layer height, roughly 1 km). Simulation of an ABL on a reasonably large domain would require an enormous amount of gridboxes, at least 10^{18}. Computational resources are by far too small to make simulations of this kind possible, now or anywhere in the (near) future.
A solution to this problem is found in Reynolds-averaging. Applying this technique to the Navier-Stokes equations, (2.37), the Reynolds-Averaged Navier-Stokes (RANS) equations are obtained. Solving these equations numerically is much faster than the DNS method. The price that has to be paid is the high amount of modeling and the loss of information on individual thermals. Therefore, this method is not fit for atmospheric

research in general. A solution that has a sort of intermediate character is Large Eddy Simulation (LES).
In LES, the largest length scales are separated from the smallest. The idea behind this is that the behaviour of large eddies is very dependent on the geometry of the specific problem, while the very smallest eddies show some universality, which makes them less dependent on the specific problem. Furthermore, at very high Reynolds numbers, a separation of length scales is also observed in terms of energy. Turbulent eddies with large length scales are associated with production of energy, while the small eddies mainly *dissipate* energy. The two ranges are separated by an inertial subrange (Pope, 2005).

2.3.1 Filtered equations

To achieve the separation of length scales a filtering operator is applied onto the governing equation. This filter can be written as follows:

$$\widetilde{\varphi}\left(\vec{x},t\right) = \int G\left(\vec{r},\vec{x}\right)\varphi\left(\vec{x}-\vec{r},t\right)\mathrm{d}\vec{r}. \tag{2.39}$$

Here $\widetilde{\varphi}$ is a filtered variable, that is (still) a function of position $\vec{x}$ and time t, G is a normalized filter function and $\vec{r}$ is a position vector that is integrated over. Unlike the general filter, a homogeneous filter is no function of $\vec{x}$. The difference between the 'real' variable and the filtered one is called the residual φ'':

$$\varphi'' = \widetilde{\varphi} - \varphi. \tag{2.40}$$

Note that there are many different notations for these filtered and residual variables. A tilde is used for the former instead of an overbar to make the distinction between Reynolds-Averaging and filtering. The double prime instead of a single, is also to make the distinction between a deviation from an average and the residual. Filtering is fundamentally different from averaging, which should be kept in mind.
Applying the filter to the continuity equation, equation (2.32), results in:

$$\widetilde{\frac{\partial u_j}{\partial x_j}} = \frac{\partial \widetilde{u_j}}{\partial x_j} = 0. \tag{2.41}$$

Here, a homogeneous filter is used, which justifies the interchange of the derivation and filtering operator. The filtered equation for conservation of a quantity $\varphi \in \{q_t, \theta_l\}$ is as follows:

$$\frac{\partial \widetilde{\varphi}}{\partial t} + \frac{\partial \widetilde{u_j\varphi}}{\partial x_j} = \widetilde{S_\varphi}. \tag{2.42}$$

If the definition: $\widetilde{u_j\varphi} - \widetilde{u_j}\widetilde{\varphi} = \tau_j^{(\varphi)}$ is used to substitute out $\widetilde{u_j\varphi}$, the result is (Lesieur et al., 2005):

$$\frac{\partial \widetilde{\varphi}}{\partial t} + \frac{\partial \widetilde{u_j}\widetilde{\varphi}}{\partial x_j} = -\frac{\partial \tau_j^{(\varphi)}}{\partial x_j} + \widetilde{S_\varphi}. \tag{2.43}$$

The defined variable $\tau_j^{(\varphi)}$ is the subfilter scalar flux, which, using equation (2.40), can be written as:

$$\tau_j^{(\varphi)} = \widetilde{u_j''\varphi''} + \widetilde{\widetilde{u_j}\varphi''} + \widetilde{u_j''}\widetilde{\varphi} + \widetilde{\widetilde{u_j}\widetilde{\varphi}} - \widetilde{u_j}\widetilde{\varphi}. \tag{2.44}$$

This equation can also be used to include passive scalars, such as concentrations of chemical species or smoke/tracer particles. It is interesting to note that when a Reynolds averaging filter is used over a grid volume, the second and the third term of the equation are zero. Furthermore, the last two terms cancel, so the subfilter scalar flux equals the filtered (=grid volume averaged) product of the residual of u_j and of φ:

$$\tau_j^{(\varphi)} = \widetilde{u_j''\varphi''}. \tag{2.45}$$

Note that this may be true for specific filters, but certainly not in general. In all cases, the subfilter fluxes have to be modelled by subfilter scale (SFS) parametrization in LES models.

The momentum equation is treated quite similarly. In this equation, however, there are some extra terms and effects that have to be taken into account. The result of filtering equation (2.37) is given below:

$$\widetilde{\rho}\left(\frac{\partial \widetilde{u_i}}{\partial t} + \frac{\partial \widetilde{u_j u_i}}{\partial x_j}\right) = -\frac{\partial \widetilde{p}}{\partial x_i} - \delta_{i3}\widetilde{\rho}g - 2\widetilde{\rho}\epsilon_{ijk}\omega\eta_j\widetilde{u_k}. \tag{2.46}$$

Again, the second term on the lhs is substituted out, now using the residual-stress tensor τ_{ij}:

$$\widetilde{\rho}\left(\frac{\partial \widetilde{u_i}}{\partial t} + \frac{\partial \widetilde{u_j}\widetilde{u_i}}{\partial x_j}\right) = -\widetilde{\rho}\frac{\partial \tau_{ij}}{\partial x_j} - \frac{\partial \widetilde{p}}{\partial x_i} - \delta_{i3}\widetilde{\rho}g - 2\widetilde{\rho}\epsilon_{ijk}\omega\eta_j\widetilde{u_k}, \tag{2.47}$$

in analogy with the Reynolds stress tensor in the RANS equations. It is good to note that this stress tensor is entirely due to the filtering process. It acts more or less as a bridge between the SFS and the filtered contributions.
To arrive at the actual LES equations, yet another approximation is used. The assumption here is that the temperature varies around a mean or reference temperature T_0 with small deviations. Thus, the same happens for $\widetilde{\rho}$:

$$\widetilde{\rho} = \rho_0 + \rho' \qquad \text{where:} \quad \rho' \ll \widetilde{\rho}. \tag{2.48}$$

Now, since deviations from $\rho_0 = \rho(T_0)$ are small, a Taylor expansion around T_0 can be used:

$$\widetilde{\rho}(T_v) = \rho_0 + \frac{\partial \rho}{\partial T_v}\Big|_{T_v=T_0}(T_v - T_0), \tag{2.49}$$

where higher order terms are neglected and the virtual potential temperature is used. To evaluate the last term, the ideal gas law, as written in equation (2.10), is used:

$$\widetilde{\rho}(T_v) = \rho_0 - \frac{(T_v - T_0)p}{R_d T_0^2} = \rho_0 - \frac{T_v - T_0}{T_0}\rho_0. \tag{2.50}$$

For the pressure, something similar is assumed: the filtered pressure is a sum of a reference pressure p_0 and some smaller deviation p'. Using hydrostatic equilibrium, equation (2.1), the pressure term on the rhs of equation (2.47) can be rewritten in the following form:

$$\frac{\partial \widetilde{p}}{\partial x_i} = \frac{\partial p'}{\partial x_i} - \delta_{i3}\rho_0 g. \tag{2.51}$$

Finally, equation (2.50) is used in equation (2.47) to substitute out $\widetilde{\rho}$ in every term but the gravitational. The fluctuating part of ρ is in all cases neglected. Furthermore, equation (2.51) is used to replace the pressure term, giving:

$$\rho_0 \left(\frac{\partial \widetilde{u_i}}{\partial t} + \frac{\partial \widetilde{u_j}\widetilde{u_i}}{\partial x_j} \right) = -\rho_0 \frac{\partial \tau_{ij}}{\partial x_j} - \frac{\partial p'}{\partial x_i} + \delta_{i3}\rho_0 g - \delta_{i3}\widetilde{\rho} g - 2\rho_0 \epsilon_{ijk}\omega\eta_j \widetilde{u_k}, \tag{2.52}$$

The third and fourth term on the rhs of this equation are very similar and can be merged. Then, equation (2.50) can again be used to substitute out $\widetilde{\rho}$. This time, however, due to the size of g, the fluctuating part cannot be neglected. Dividing the result by ρ_0 gives:

$$\frac{\partial \widetilde{u_i}}{\partial t} + \frac{\partial \widetilde{u_j}\widetilde{u_i}}{\partial x_j} = -\frac{\partial \tau_{ij}}{\partial x_j} - \frac{1}{\rho_0}\frac{\partial p'}{\partial x_i} - \frac{\widetilde{\theta_v} - \theta_0}{\theta_0}\delta_{i3} g - 2\epsilon_{ijk}\omega\eta_j \widetilde{u_k}, \tag{2.53}$$

where equation (2.7) was used to write potential temperature instead of T_v. The approximation used above, where the density fluctuations are neglected in all terms but the gravitational, is called the Boussinesq approximation. It is widely used and believed to be very accurate in the case of shallow boundary layers.

2.3.2 Closure

As was already noted before, SFS fluxes need to be parametrized to close equations (2.43) and (2.53). In the case of the scalar SFS flux, this is done by introducing a diffusivity constant K_φ and writing:

$$\tau_j^{(\varphi)} = -K_\varphi \frac{\partial \widetilde{\varphi}}{\partial x_j}, \tag{2.54}$$

where in DALES $K_{q_t,\theta_l} = K_h$ is used. Doing the same for τ_{ij} would give:

$$\tau_{ij} = -K_m \left(\frac{\partial \widetilde{u_i}}{\partial x_j} + \frac{\partial \widetilde{u_j}}{\partial x_i} \right), \tag{2.55}$$

Here however, an inconsistency arises. In the case of homogeneous, isotropic turbulence, only the normal stresses τ_{ii} are nonzero, while the shear stress terms τ_{ij} are zero (Deardorff, 1973). Summing both sides of equation (2.55) with $i = j$ yields zero on the rhs (using the continuity equation), while on the lhs a nonzero value is found. To avoid this problem, a term involving the SFS turbulent kinetic energy $\widetilde{e} = 1/3(\widetilde{u'^2} + \widetilde{v'^2} + \widetilde{w'^2})$ is subtracted from the diagonal elements of τ_{ij}. This is compensated by adding the same term to the pressure term:

$$\tau_{ij}^{an} = \tau_{ij} - \frac{2}{3}\delta_{ij}\widetilde{e} \tag{2.56}$$

$$\pi = \frac{p'}{\rho_0} + \frac{2}{3}\widetilde{e}, \tag{2.57}$$

where π is a modified pressure and τ_{ij}^{an} is the anisotropic residual-stress tensor. In this process, the terms are splitted into an isotropic and an anisotropic part, which was first done by Deardorff (1973). The final form of the momentum equation is, using the above substitutions:

$$\frac{\partial \widetilde{u_i}}{\partial t} + \frac{\partial \widetilde{u_j}\widetilde{u_i}}{\partial x_j} = -\frac{\partial \tau_{ij}^{an}}{\partial x_j} - \frac{\partial \pi}{\partial x_i} - \frac{\widetilde{\theta_v} - \theta_0}{\theta_0}\delta_{i3} g - 2\epsilon_{ijk}\omega\eta_j \widetilde{u_k}. \tag{2.58}$$

In DALES, π is solved by writing a Poisson equation based on this equation. Using the continuity equation, the time-derivative of the velocity drops out and π can be found. Because of the periodic boundary conditions used in the horizontal directions, a Fast Fourier Transform (FFT) can be used to solve the equation in these directions. In the vertical direction, a tridiagonal system is solved (see Heus et al., 2009).

The only unknowns left in the entire system of LES-equations are the eddy diffusivity coefficients K_h and K_m. The problem of finding these is the closure problem, for which there are two commonly used models: the Smagorinsky model and the one using the SFS turbulent kinetic energy $\widetilde{e}$. The latter method is used in DALES. The assumption here is that K_h and K_m are functions of $\widetilde{e}$ and some lengthscale. To find $\widetilde{e}$ another budget equation is written and solved:

$$\frac{\partial \widetilde{e}}{\partial t} + \widetilde{u}_j \frac{\partial \widetilde{e}}{\partial x_j} = -\tau_{ij}^{an} \frac{\partial \widetilde{u}_i}{\partial x_j} + \frac{g}{\theta_0} \tau_3^{\theta_v} - \frac{\partial \tau_j^e}{\partial x_j} - \frac{1}{\rho_0} \frac{\partial \tau_j^p}{\partial x_j} - \varepsilon, \tag{2.59}$$

where $\tau_j^{(\varphi)}$ are the residual scalar fluxes as before and ε is the dissipation rate of Turbulent Kinetic Energy (TKE). The second term on the lhs is the only one that can be considered known. The terms on the rhs need all be modeled in some way. Here, the main equations are given. For a more detailed treatment of the TKE-budget equation and it's modeling, see e.g. Van Zanten (2000) or Stull (1993). The discussion below is more or less a summary of Heus (2008).
In the first term on the rhs can be parametrized using equation (2.56), while the production due to buoyancy, the second term, can be rewritten in terms of $\tau_3^{q_t}$ and $\tau_3^{\theta_l}$ (see section 2.1.2). These fluxes can in turn be parametrized using equation (2.54). The third and the fourth term are parameterized using:

$$-\frac{\partial}{\partial x_j} \left(\tau_j^e + \frac{1}{\rho_0} \tau_j^p \right) = 2K_m \frac{\partial \widetilde{e}}{\partial x_j}. \tag{2.60}$$

The last remaining term is the dissipation, which is the energy loss per unit of time due to viscous effects on the smallest scale. An expression for the dissipation is found by summation of the effect over all wavenumbers below the inertial subrange. Doing this eventually yields:

$$\varepsilon = \widetilde{e}^{3/2} k_f \left(\frac{3}{2} \alpha \right)^{-3/2}, \tag{2.61}$$

where k_f is the filter wavenumber and $\alpha = 1.5$ is the Kolmogorov constant.
Now, to find K_h, and K_m, the production of TKE is equated locally to the dissipation. The result of this is an expression for K_m and K_h is directly written in a similar form:

$$K_{m,h} = c_{m,h} \lambda \widetilde{e}^{1/2}, \tag{2.62}$$

with c_m and c_h parametrization constants, given by:

$$c_{m,h} = \frac{c_f}{2\pi} \left(\frac{3}{2} \alpha \right)^{-3/2}. \tag{2.63}$$

Here, a parametrization constant c_f is used that involves the filtering properties. The filterwidth, namely, is defined as:

$$c_f \lambda = \frac{2\pi}{k_f}. \tag{2.64}$$

Above, λ is in units of length and is usually chosen proportional to the gridsize: $\lambda = \sqrt[3]{\Delta x \Delta y \Delta z} \equiv \Delta$. This way, the filter width is made proportional to the gridsize. For this parametrization it seems important that the gridsize is chosen correctly, to make sure that k_f lies inside the inertial subrange.
Using the variables defined above, the equation for the dissipation (2.61) can also be rewritten:

$$\varepsilon = \frac{c_\varepsilon}{\lambda} \widetilde{e}^{3/2}, \tag{2.65}$$

with

$$c_\varepsilon = \frac{2\pi}{c_f} \left(\frac{3}{2} \alpha \right)^{-3/2}. \tag{2.66}$$

The subject of this research is mainly a stratocumulus topped BL, which has special properties discussed in the first chapter of this thesis. One of these properties is of specific interest in the light of the SFS parametrization. At the top of the BL, a strong, stable inversion is found. Due to the stability, the use of the SFS-closure as defined above is not appropriate. The mixing lengths are very small in this regime and setting it proportional to the gridsize is not sufficient any longer. Therefore, a stability correction is used, which adjusts λ where necessary:

$$\lambda = \min \left(\Delta, c_N \frac{\widetilde{e}^{1/2}}{N} \right), \tag{2.67}$$

where $N^2 = \frac{g}{\theta_0} \frac{\partial \theta_v}{\partial z}$ is the so-called Brunt-Väisälä frequency and c_N is a constant. Stability corrections are also applied on the coefficients c_h and c_ε:

$$c_h = \left(c_{h,1} + c_{h,2} \frac{\lambda}{\Delta} \right) c_m, \tag{2.68}$$

$$c_\varepsilon = c_{\varepsilon,1} + c_{\varepsilon,2} \frac{\lambda}{\Delta}. \tag{2.69}$$

Now, all LES-equations are closed, leaving a set of free parameters. The values that are used in DALES can be found in table 2.2.

Table 2.2: The free parameters used in the SFS model of DALES.

α	c_f	$c_{\varepsilon,1}$	$c_{\varepsilon,2}$	c_m	$c_{h,1}$	$c_{h,2}$	c_N
1.5	2.5	0.19	0.51	0.12	1	2	0.76

2.3.3 Source/sink terms

The model as it is described in the previous section is not complete without a proper description of the source/sink terms for each variable φ, in equation (2.43) denoted by S_φ. Three different processes have to be described by this term: longwave radiative cooling, absorption of shortwave radiation and precipitation.
Both radiation processes are described by a single term:

$$S^R_{\theta_l} = \frac{\partial F_R}{\partial z}, \tag{2.70}$$

where F_R is the net radiative flux. The longwave part of this flux is parametrized by:

$$F_{R,lw}(z) = \Delta F_{R,lw} \exp\left[-kW(z, z_i)\right], \tag{2.71}$$

where $\Delta F_{R,lw}$ is the longwave radiative jump at cloud top, $W(z, z_i)$ is the liquid water path between the inversion and height z and $k = 130$ m^2 kg^{-1} is the absorption coefficient. Longwave radiative warming at cloud base is neglected.
The effect of shortwave radiation is much more complicated to implement. First of all, the downwelling shortwave radiation is a function of the position on earth and of time. These effects are easily described. However, the interaction of cloud droplets with the radiation of different wavelengths is not. In DALES, a delta-Eddington approximation is used. A description of this approximation can for instance be found in Duynkerke et al. (2004).

When microphysics are included in the simulations, the scheme of Khairoutdinov and Kogan (2000) is used (in the remainder of this thesis: KK). This parametrization scheme is specifically developed for the use in the LES modeling of STBLs. The idea of the parametrization is the separation of liquid water inside the cloud into droplets with a small diameter ($< 20\mu$m), called cloud droplets, and larger rain droplets. The approach is usually referred to as (Kessler-type) bulk microphysics. It originates from the fact that the cloud droplets mainly grow by condensation, while the larger droplets, which tend to fall down under the influence of gravity, grow by collecting other droplets in their path, a process called accretion.
A problem with bulk microphysics is that the rate at which rain water is produced from cloud water has to be parametrized, a process entirely due to the artificial split of drop sizes. Of course, many other conservation equations have to be solved to described the cloud drop concentration, the cloud liquid water content, the rain drop concentration, the rain liquid water content, the total concentration of cloud condensation nuclei (CCN) and the integral radius of cloud droplets, which is an important quantity for the radiative properties of clouds. These equations contain source and sink terms for all kinds of processes, from condensation and activation to accretion and autoconversion.
In the scheme developed by KK, these source and sink terms are parametrized on the basis of simulations of STBLs using an explicit microphysics scheme. The bulk microphysics scheme is shown to be capable of reproducing the results of the explicit scheme reasonably well, while requiring much less computational effort. Nevertheless, the scheme is expensive: simulations with bulk microphysics in DALES require up to 50% extra computational time compared to simulations without.
Another, more widely applicable, bulk microphysics scheme is that developed by Seifert and Beheng (2001). This scheme has a less empirical background and can also be used in Cu simulations. A short description is included in the DALES model description.
Finally, geostrophic wind and subsidence are also included as source terms, as they are (in general) a function of height and they act everywhere in the domain. Subsidence is for instance modeled by prescribing a mean velocity $\overline{w}$, resulting in a source/sink term:

$$\widetilde{S}_{\varphi}^{subs} = \overline{w}\frac{\partial \widetilde{\varphi}}{\partial z}. \tag{2.72}$$

2.4 Mixed layer model

Compared to DNS, LES models are a big step forward in terms of computational cost. Simulations of several hours or even several days are possible on (super)computers nowadays, provided the resolution is chosen appropriately. However, for some applications, this is just not good enough. LES is for instance still far to expensive to use as a subgrid model in weather forecasting models. Furthermore, a single simulation is usually not enough to draw general conclusions. Perturbation studies for instance, require many simulations with slightly different initial conditions to find out how these changes influence BL behaviour. Since there are so many different initial conditions and BL forcings possible, LES is still expensive.
Therefore, a MLM can be very interesting. The computational time for a simulation of several days need not be more than a few seconds. An accurate MLM can therefore be of inestimable value. Thousands of model runs can be done on a simple pc, giving a certain degree of insight that several LES runs cannot give.
A drawback of a simpler model is, however, that it is not always applicable, due to more binding assumptions. The danger is that the model results are used in unfit situations, leading to completely wrong conclusions.
In this section, the model equations are derived from the governing equations as given in section 2.2. At each step, the assumptions are explicitly mentioned. Again, the source/sink terms are discussed and the section ends with a description of entrainment and it's parametrization in MLMs.

2.4.1 Model equations

The starting point of the derivation of the model equations of the MLM are the governing equations for conserved variables or passive scalars as given by equation (2.38), which is repeated here for convenience:

$$\frac{\partial \varphi}{\partial t} + \frac{\partial \varphi u_j}{\partial x_j} = S_\varphi.$$

There are 3 steps involved in deriving the budget equations of the MLM. First of all, the assumption of horizontal homogeneity is used. Since Sc clouds form large fields, this assumption is not hard to defend. Large parts seem to be homogeneous at a large scale. Furthermore, measurements taken during aircraft flights are, due to the aircraft's high horizontal velocity, also horizontally averaged. The second step is then to average the equations over the horizontal directions using Reynolds-averaging, given by:

$$\varphi = \overline{\varphi} + \varphi', \tag{2.73}$$

where a quantity is decomposed in an average contribution $\overline{\varphi}$ and a deviation from that average φ'. For $\overline{\varphi}$ the average in the horizontal directions is taken. Applying this procedure to the general equation yields:

$$\frac{\partial \overline{\varphi}}{\partial t} + \frac{\partial \overline{u_j \varphi}}{\partial x_j} = \overline{S_\varphi}. \tag{2.74}$$

Like in the derivation of the LES model equations, the second term is decomposed:

$$\frac{\partial \overline{\varphi}}{\partial t} + \frac{\partial \overline{u_j}\,\overline{\varphi}}{\partial x_j} = -\frac{\partial T_j^{(\varphi)}}{\partial x_j} + \overline{S_\varphi}, \tag{2.75}$$

where $T_j^{(\varphi)} = \overline{u_j \varphi} - \overline{u_j}\,\overline{\varphi}$ is the flux due to the deviations from the average. This flux can also be written as:

$$T_j^{(\varphi)} = \overline{u_j' \varphi'} + \overline{\overline{u_j}\,\varphi'} + \overline{u_j' \overline{\varphi}} + \overline{\overline{u_j}\,\overline{\varphi}} - \overline{u_j}\,\overline{\varphi}. \tag{2.76}$$

Since a Reynolds-averaging filter is used, unlike the general filter with LES, the second and third term on the rhs are both zero, while the fourth and fifth term add up to zero. The equation is reduced to: $T_j^{(\varphi)} = \overline{u_j' \varphi'}$. This quantity will be referred to as the turbulent flux. Due to the horizontal homogeneity, the influence of the turbulent fluxes in the horizontal plane are expected to even out in time, therefore, of this turbulent flux, only $\overline{w'\varphi'}$ is nonzero. Equation 2.75 reduces to:

$$\frac{\partial \overline{\varphi}}{\partial t} + \frac{\partial \overline{u_j}\,\overline{\varphi}}{\partial x_j} = -\frac{\partial \overline{w'\varphi'}}{\partial x_j} + \overline{S_\varphi}. \tag{2.77}$$

The second term on the rhs can be expanded using the product rule of differentiation to give:

$$\frac{\partial \overline{u_j}\,\overline{\varphi}}{\partial x_j} = \frac{\partial \overline{u}\,\overline{\varphi}}{\partial x} + \frac{\partial \overline{v}\,\overline{\varphi}}{\partial y} + \frac{\partial \overline{w}\,\overline{\varphi}}{\partial z} = \overline{u}\frac{\partial \overline{\varphi}}{\partial x} + \overline{v}\frac{\partial \overline{\varphi}}{\partial y} + \overline{w}\frac{\partial \overline{\varphi}}{\partial z} + \overline{\varphi}\left(\frac{\partial \overline{u}}{\partial x} + \frac{\partial \overline{v}}{\partial y} + \frac{\partial \overline{w}}{\partial z}\right). \tag{2.78}$$

The term between brackets is zero by the continuity equation, while the assumption of horizontal homogeneity implies that horizontal gradients in φ are zero. Therefore, only the last term on the rhs is left and equation 2.77 reduces to:

$$\frac{\mathrm{d}\overline{\varphi}}{\mathrm{d}t} + \overline{w}\frac{\partial \overline{\varphi}}{\partial z} = -\frac{\partial \overline{w'\varphi'}}{\partial z} + \overline{S_\varphi}. \tag{2.79}$$

To rewrite the partial derivative of the first term on the lhs into a total derivative, a Lagrangian way of measuring is assumed, in which a column of air is followed that travels with the mean wind. This way, contributions of large scale advection of a quantity can be neglected.
The third and last step is the most interesting, the model also gets its name from it. The entire BL is assumed to be well-mixed by turbulence, which means that a conserved variable has a constant mean value over the entire boundary layer. This means that the mean vertical gradient of φ is zero and thus, the second term on the lhs of equation (2.79) is also zero, giving:

$$\frac{\mathrm{d}\overline{\varphi}}{\mathrm{d}t} = -\frac{\partial \overline{w'\varphi'}}{\partial z} + \overline{S_\varphi}, \tag{2.80}$$

inside the BL. Under the mixed layer assumption, equation (2.79) can easily be integrated over the BL:

$$z_i \frac{\mathrm{d}\varphi_{ml}}{\mathrm{d}t} = -\left(\overline{w'\varphi'}\big|_{z_i} - \overline{w'\varphi'}\big|_0\right) + \int_0^{z_i} \overline{S_\varphi}\mathrm{d}z, \tag{2.81}$$

in which $\overline{w'\varphi'}\big|_z$ is the flux of φ at height z and z_i is the height of the boundary layer. Furthermore, φ_{ml} denotes the BL averaged value of φ. This equation is the budget equation for both BL averaged variables, $q_{t,ml}$ and $\theta_{l,ml}$. Unknowns in the equation are z_i, $\overline{w'\varphi'}\big|_{z_i}$ and $\overline{w'\varphi'}\big|_0$, ignoring the source/sink terms for the moment.

The surface fluxes can fairly accurately be determined. Furthermore, several parametrizations can be used to represent this term based on the SST. A simple one, that is easily implemented in the MLM is:

$$\overline{w'\varphi'}\big|_0 = C_D|\vec{U}|(\varphi_{surf} - \varphi_{ml}), \tag{2.82}$$

in which φ_{surf} is the value of φ directly at the surface, $|\vec{U}|$ is the absolute velocity relative to the surface and C_D is an exchange coefficient, which is parametrized by Wakefield and Schubert (1981):

$$C_D = 0.001(1 + 0.07|\vec{U}|). \tag{2.83}$$

The value of θ_l at the surface is given by division of the SST by the Exner function, while $q_{t,surf}$ is the saturation value q_s at SST and surface pressure.
The turbulent flux at z_i can be written using an approximate relation derived by Lilly (1968):

$$\overline{w'\varphi'}\big|_{z_i} = -w_e\Delta\varphi, \tag{2.84}$$

where $\Delta\varphi$ denotes the difference between φ_{ml} and $\overline{\varphi}$ just above the inversion, also called the 'jump' of φ. This result is usually referred to as the 'flux-jump relation' and it is exact for an infinitesimally thin inversion layer.
Now in the FA, where turbulence is absent and sink/source terms are negligible, equation (2.79) reduces to:

$$\frac{\mathrm{d}\overline{\varphi}}{\mathrm{d}t} + \overline{w}\frac{\partial\overline{\varphi}}{\partial z} = 0. \tag{2.85}$$

Here, $\overline{w}$ is the mean vertical wind caused by subsidence. When assuming that the divergence of air in the horizontal plane D is constant with height, $\overline{w}$ is given by:

$$\overline{w} = -Dz. \tag{2.86}$$

Subsidence, that pushes on top of the BL, and entrainment, which pulls air into the BL, together control the evolution of the BL height:

$$\frac{\mathrm{d}z_i}{\mathrm{d}t} = \overline{w} + w_e. \tag{2.87}$$

Now the evolution of the mean state of the BL is determined by initial conditions, source/sink terms and forcings (surface conditions and subsidence) together with the entrainment velocity, which is said to close the system of equations.

2.4.2 Entrainment

The entrainment rate is of large influence on the BL values of both q_t and θ_l through the top fluxes and it also controls the BL growth. Figure 4.1 shows that small differences in the entrainment rate can cause visible differences in BL height, even after a short period of 3 hours. A good representation in the MLM is therefore important.
There are several ways of dealing with the entrainment and the method used depends mostly on the purpose a researcher has with the MLM. For instance, running the model for different values of the entrainment rate, gives different profiles. Fitting these results

to measurements and selecting the best fit, allows to diagnose a value for the entrainment rate. This way, the model is used as a diagnostic tool (Duynkerke et al., 1995). However, DALES already diagnoses the entrainment rate. These results can also be used as input to the MLM. As long as all assumptions, made in the model, are valid, the results will be very close to the LES results. The comparison gives the opportunity to find out under what conditions the assumptions fail and thus under what conditions the MLM may be used.
A last option is to use an entrainment parametrization. The object of this parametrization is to calculate the entrainment rate on the basis of BL conditions:

$$w_e = f\left(\Delta q_t, \Delta\theta_l, \overline{w'\theta_l'}\big|_0, \overline{w'q_t'}\big|_0, \mathrm{D}F_R, z_b, z_t\right), \tag{2.88}$$

where z_t is cloud top height. Using parametrization, the MLM is closed and it can be used entirely independent of measurements or LES. Comparison with LES and measurements can then give a good image of the strengths and weaknesses of the model.
The accuracy of existing parametrizations is questionable. Most of the parametrizations are made to fit a series of observations or LES results. While sometimes doing a good job in these experiments, general use mostly results in large differences between different parametrizations, up to factors of two.
In the MLM, parametrizations of Moeng (Moeng, 2000) and Nicholls and Turton (Turton and Nicholls, 1987) are implemented. Moeng (CM) used LES results to arrive at her parametrization:

$$w_e = \frac{0.2\rho_0 c_p \overline{w'\theta_l'}\big|_0 + \mathrm{D}F_R\left[2.5 - 2\exp(-b_m\sqrt{W})\right]}{\rho_0 c_p \Delta\theta_l}, \tag{2.89}$$

where $b_m = 0.9\ \mathrm{m}^2\ \mathrm{kg}^{-1}$ is a parameter.
The parametrization by Nicholls and Turton (NT) is somewhat more complicated. Their starting point is the parametrization used for convective BLs:

$$\frac{w_e}{w^*} = \frac{A}{\mathrm{Ri}_{w^*}}, \tag{2.90}$$

where A is a constant and

$$w^{*3} = \frac{2.5g}{\theta_0}\int_0^{z_i} \overline{w'\theta_v'}\mathrm{d}z \tag{2.91}$$

is the convective velocity scale. The Richarson number is based on the convective velocity scale and is given by:

$$\mathrm{Ri}_{w^*} = \frac{gz_i}{\theta_0}\frac{\Delta\theta_v}{w^{*2}}. \tag{2.92}$$

For a clear convective BL with heating from below, a good representation of the entrainment rate is found for $A = 0.2$. In Sc clouds however, processes like evaporation and longwave radiative cooling play a large role in the dynamics, resulting in entrainment rates a factor 10 higher. In NT, the constant A is parametrized as:

$$A_{NT} = 0.2\left[1 + a_2\left(1 - \frac{\Delta\theta_{v,NT}}{\Delta\theta_v}\right)\right]. \tag{2.93}$$

In this equation, a_2 is a constant, initially suggested to be 60. However, a value $a_2 = 30$ is also sometimes used (Stevens, 2002). Finally, $\Delta\theta_{v,NT}$ is a short of effective θ_v (buoyancy) jump over the inversion, given by twice the sum of all possible virtual potential temperature jumps that can be found by mixing BL air with air from above the inversion. An analytic expression of this term can be given from geometric considerations of a mixing diagram as found in figure 3 of Stevens (2002). Both parametrizations are intrinsically very different. That of Moeng is mostly based on experiments and it values the radiative cooling as the most influential process. That of NT is mainly based on the (vertically integrated) buoyancy flux. This is also shown by Stevens (2002). He showed that most commonly used parametrizations can be written in a single format, that clearly shows the differences but also the agreements between them. The format is given by

$$w_e = \mathfrak{A}\frac{\mathfrak{W}}{\Delta\theta_v} + \mathfrak{D}, \tag{2.94}$$

in which the Gothic symbols are used for terms that are dependent of the parametrization used: $\mathfrak{A}$ is an efficiency of entrainment generation by turbulence, $\mathfrak{W}$ is a work term associated with turbulent processes and $\Delta\theta_v$ is the isentropic jump of θ_v over the inversion. The last term in the equation, $\mathfrak{D}$ represents non-turbulent processes.
For the entrainment parametrization of NT, $\mathfrak{D}$ is found to be zero, while $\mathfrak{A}$ is given by:

$$\mathfrak{A} = \frac{A_{NT}}{20 + \mu A_{NT}}, \tag{2.95}$$

where A_{NT} is again the constant given by equation (2.93), while μ measures the importance of top-down turbulent fluxes and is given by:

$$\mu = \frac{\Delta_d\theta_v}{\Delta\theta_v}\frac{z_b}{z_i} + \frac{\Delta_w\theta_v}{\Delta\theta_v}\left(1 - \frac{z_b}{z_i}\right). \tag{2.96}$$

Here, $\Delta_d\theta_v$ and $\Delta_w\theta_v$ are, respectively, the dry and the moist buoyancy jump over the inversion given by:

$$\Delta_{d,w}\theta_v = A_{d,w}\Delta\theta_l + B_{d,w}\Delta q_t. \tag{2.97}$$

Finally, the work term $\mathfrak{W}$ in equation (2.94) is the vertical integral of the θ_v profile, making buoyancy the entrainment producing mechanism, which shows clearly the difference with the parametrization of CM. Here, the work term is made up entirely by the $\overline{w'\theta_l'}$ and the radiative cooling at the top. Furthermore, $\mathfrak{A}$ is small. On the other hand, $\mathfrak{D}$ plays a significant role.
That the parametrizations are very different also follows from figure 2.1. The CM parametrization shows only dependence on the jump of θ_l. An advantage is, however, that the entrainment is defined for all combinations of $\Delta\theta_l$ and Δq_t. The entrainment as found from NT seems more realistic due to dependency on both variables. However, asymptotic behaviour is found beyond which unrealistic, negative entrainment rates are found. This behaviour, however, is only found in the lower left bottom. Under these conditions, most likely only Cu clouds will be found. The mixed layer approximation is expected to have failed long before these conditions are reached.

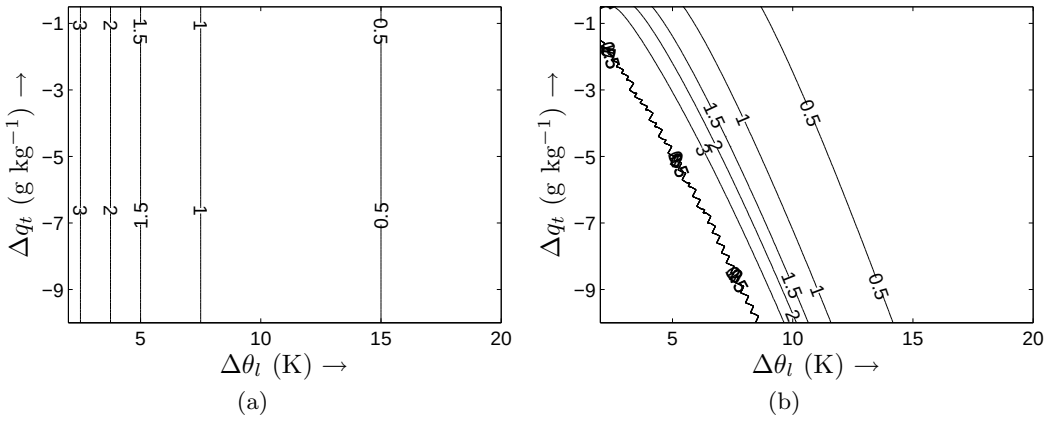

Figure 2.1: The entrainment in cm s^{-1} as a function of the inversion jumps $\Delta\theta_l$ and Δq_t for the parametrization of Moeng (a) and that of Nicholls and Turton (b). Moeng's parametrization clearly shows no dependends of Δq_t, while that of NT shows asymptotic behaviour. The profiles of θ_l and q_t can be found in equation (3.2), while the boundary conditions are given in table 3.2. LWP, z_b and $q_{l,max}$ are diagnosed by the MLM and are 160.8 g m^{-2}, 352.2 m and 0.70 g kg^{-1} respectively at $t = 0$ s.

2.4.3 Source/sink terms

Up until now, processes for which q_t and θ_l are not conserved have been neglected. For processes like freezing and melting this is not a problem, since low-level clouds are usually not cold enough to contain any ice. However, in the introduction, it was already made clear that radiation plays an important role and it is assumed that precipitation also plays a significant role in especially decoupling of the BL. These two processes are included by appropriate source/sink terms.
Radiation is represented by the following term:

$$\int_0^{z_i} S_{\theta_l}^R \mathrm{d}z = -\frac{1}{c_p \rho_0} \mathrm{D}F_R. \tag{2.98}$$

In this equation, $\mathrm{D}F_R$ is the sum of the contributions of both longwave and shortwave radiation:

$$\mathrm{D}F_R = \mathrm{D}F_{R,lw} + \mathrm{D}F_{R,sw}. \tag{2.99}$$

Furthermore, the capital D denotes a difference between the boundary layer top and the surface: $\mathrm{D}F = F|_{z_i} - F|_0$. The longwave radiative part of $\mathrm{D}F_R$ is found from measurements, during ASTEX the cooling was about 74 W m^{-2} over the top 40 meters of the BL. The slight warming at cloud bottom, due to the temperature difference between the cloud and the surface, is neglected here as well as in the LES model.
Including shortwave radiation is a different story. The amount of downwelling shortwave radiation depends on time, the day of the year and location on earth (latitude and longitude). The angle of the sun with respect to the normal to the earth's surface is relatively easily calculated in a few steps, given among others in Boeker and van Grondelle (1999) and also used in the LES model.
The forcing is however, not given by the downwelling radiation, but by the absorption of this radiation. The method used is the sunray model (Fouquart and Bonnel, 1980) and is also the same as the one used in DALES.

Of course, it is also possible to adopt a average diurnal radiative forcing. This is for instance done by Bretherton and Wyant (1997). However, in order to look at the influence of the absorption of shortwave radiation on decoupling, it is more interesting to implement a diurnal cycle.

The other process that must be accounted for in the MLM is precipitation. An exact representation of the interaction of gravity and drag with a broad spectrum of droplet sizes is of course impossible to achieve and far from desirable in a simple model. Here the approach used by Caldwell and Bretherton (2009) is adopted. The precipitation flux at the surface is used here as an extra surface flux:

$$\int_0^{z_i} S_{\theta_l}^P \mathrm{d}z = -\frac{L}{\rho_0 c_p} F_{p,surf} \text{ and} \tag{2.100}$$

$$\int_0^{z_i} S_{q_t}^P \mathrm{d}z = \frac{1}{\rho_0} F_{p,surf}, \tag{2.101}$$

where S_φ^P is the sink term due to precipitation for the variable φ and $F_{p,surf}$ is the precipitation (or liquid water) flux at the surface in units of kg s^{-1} m^{-2}, or mm s^{-1} at a liquid water density ρ_l of 1000 kg m^{-2}. Now, $F_p(z)$ below cloud is given by:

$$F_p(z) = F_p(z_b) \exp\left[-k_p \left(\frac{z_b - z}{\overline{r}^{2.5}}\right)^{1.5}\right] \qquad \text{for } z < z_b \tag{2.102}$$

and incloud by:

$$F_p(z) = F_p(z_b) \left[1 - \left(\frac{z - zb}{zi - zb}\right)^3\right] \qquad \text{for } z < z_b \tag{2.103}$$

with

$$F_p(z_b) = -4.3 \times 10^{-6} \left(\frac{10^3 W}{N_c}\right)^{1.75} \tag{2.104}$$

as parametrized by Comstock et al. (2004). In these equations, z_b is the cloud base height, k is a constant equal to 320 μm$^{3.75}$ m$^{-1.5}$ and N_c is the droplet number concentration in cm^{-3}. Furthermore, $\overline{r} = 60\,\mu$m.
With the influence of both radiation and precipitation now modelled, the model equations can now be written:

$$z_i \frac{\mathrm{d}\theta_{l,ml}}{\mathrm{d}t} = C_D |\vec{U}| (\theta_{l,surf} - \theta_{l,ml}) + w_e \Delta\theta_l - \frac{1}{c_p \rho_0} \left(\mathrm{D}F_R - LF_{p,surf}\right); \tag{2.105}$$

$$z_i \frac{\mathrm{d}q_{t,ml}}{\mathrm{d}t} = C_D |\vec{U}| (q_{t,surf} - q_{t,ml}) + w_e \Delta q_t - \frac{1}{\rho_0} F_{p,surf}. \tag{2.106}$$

2.4.4 Turbulent fluxes at night, without precipitation

In the special case of a STBL at night, where precipitation can be neglected, the turbulent flux profiles in a MLM can be found. First of all, quasi-steady state must be assumed. This can be seen as the limit of very slowly increasing SST, slow enough to let the BL

adjust to each change entirely. The result of this assumption is that the gradient of a quantity is not time dependent:

$$\frac{\mathrm{d}}{\mathrm{d}t}\left(\frac{\partial\overline{\varphi}}{\partial z}\right) = 0. \tag{2.107}$$

Differentiation of equation (2.80) and application of this approximation yields:

$$\frac{\mathrm{d}}{\mathrm{d}z}\left(\frac{\partial\overline{\varphi}}{\partial t}\right) = -\frac{\partial^2\overline{w'\varphi'}}{\partial z^2} + \frac{\partial\overline{S_\varphi}}{\partial z} = 0, \tag{2.108}$$

which means that the gradient of the vertical turbulent flux is constant when source/sink terms are absent. The turbulent flux as a function of height is then given by:

$$\overline{w'\varphi'} = \overline{w'\varphi'}\big|_0\left(1-\frac{z}{z_i}\right) + \overline{w'\varphi'}\big|_{z_i}\left(\frac{z}{z_i}\right). \tag{2.109}$$

Since the effect of longwave radiation is only present at the top of the BL, it is easily accounted for by adding the entire contribution to the top flux, giving:

$$\overline{w'\theta_l'} = \overline{w'\theta_l'}\big|_0\left(1-\frac{z}{z_i}\right) + \left(\frac{1}{\rho_0 c_p}\mathrm{D}F_R + w_e\Delta\theta_l\right)\left(\frac{z}{z_i}\right). \tag{2.110}$$

$$\overline{w'q_t'} = \overline{w'q_t'}\big|_0\left(1-\frac{z}{z_i}\right) + w_e\Delta q_t\left(\frac{z}{z_i}\right). \tag{2.111}$$

Using equations (2.26) and (2.29), the buoyancy flux can now be calculated for the entire BL, immediately showing the usefulness of these simple relations. Again, the influence of the entrainment is clearly visible.
The effects of shortwave radiation and precipitation are much more a function of height, although they are strongest around cloud top. In section 4.3 it is shown that including precipitation effects entirely at the top also gives a reasonably good result compared to LES. Finally, the effect of shortwave radiation, which is important in the simulation of the transition (in chapter 5) is also included solely at the top of the mixed layer.

Chapter 3

Atlantic Stratocumulus Transition Experiment

In 1987, a large experimental field campaign took place in which measurements were taken in an extensive field of marine Sc off the coast of California. The experiment (FIRE) was the first in its kind. Many different measurement platforms were used, including sensors hanging from tethered balloons, satellites, aircraft flights and ground-based remote-sensing systems on a ship and on the San Nicholas Island. Large amounts of data were gathered on turbulence, mean state, microphysics, radiation and even chemistry inside the BL (Albrecht et al., 1988). The cloud conditions were considered ideal: during the entire duration of the experiment, Sc was persistent. FIRE is considered highly successful.
The second FIRE experiment, is much like the first. Again, many of the same measurement platforms were used. In the first section of this chapter, some of the specifics of the experiment are discussed. The following section is concerned with the model intercomparison cases: one case based on flight A209 and the other on flight RF06. The last section of this chapter contains the information of the new model intercomparison that covers almost the entire transition.

3.1 ASTEX Observations

FIRE was very successful in collecting observations in Sc not far off the Californian coast. However, in the subtropics, where Sc air masses are advected equatorwards by the trade winds, a transition from Sc to Cu is typically observed. The object of ASTEX was to improve the understanding on this transition and to identify the processes that are most important in it (Albrecht et al., 1995).
The ASTEX experiment took place in the northeast Pacific Ocean in June 1992. Again measurements were made using aircrafts, ground observations from an island and from ships and satellites observations. The advantage of using such a wide variety of instruments and measurement platforms is that information on all relevant scales is gathered, from large-scale features on the cloud scale (satellites and high aircraft flights) to the very smallest turbulent and microphysical scale (ground based and in-cloud aircraft flights).
ASTEX was the first atmospheric experiment to adopt a Lagrangian way of measuring, which means that a column of air was selected and followed during the following hours. All measurements are done approximately in this same column during a period of two

Table 3.1: Details of the flights undertaken during the ASTEX first Lagrangian.

Flight number	1	2	3	4	5
Flight code	RF05	A209	RF06	RF07	A210
Start (UTC)	17:19	00:32	04:51	16:27	11:11
End	21:33	04:26	10:13	21:09	13:02
Date (June 1992)	12	13	13	13	14

days. Two of these Lagrangians were performed, the first of which was in relatively clean maritime air, while the second was in a more polluted air mass.
Figure 3.1 gives a schematic overview of the first ASTEX Lagrangian. The measurements started at 17:19 UTC 12 June 1992 and continued until 13:02 UTC two days later. Five flight were undertaken during this period, indicated at the bottom of the schematic. Two different aircrafts were used, the NCAR Electra flew the first, the third and the fourth flights (coded RF05, RF06 and RF07), while a C-130 aircraft flew the other two (A209 and A210). The flights, codes and flight times are found in table 3.1.

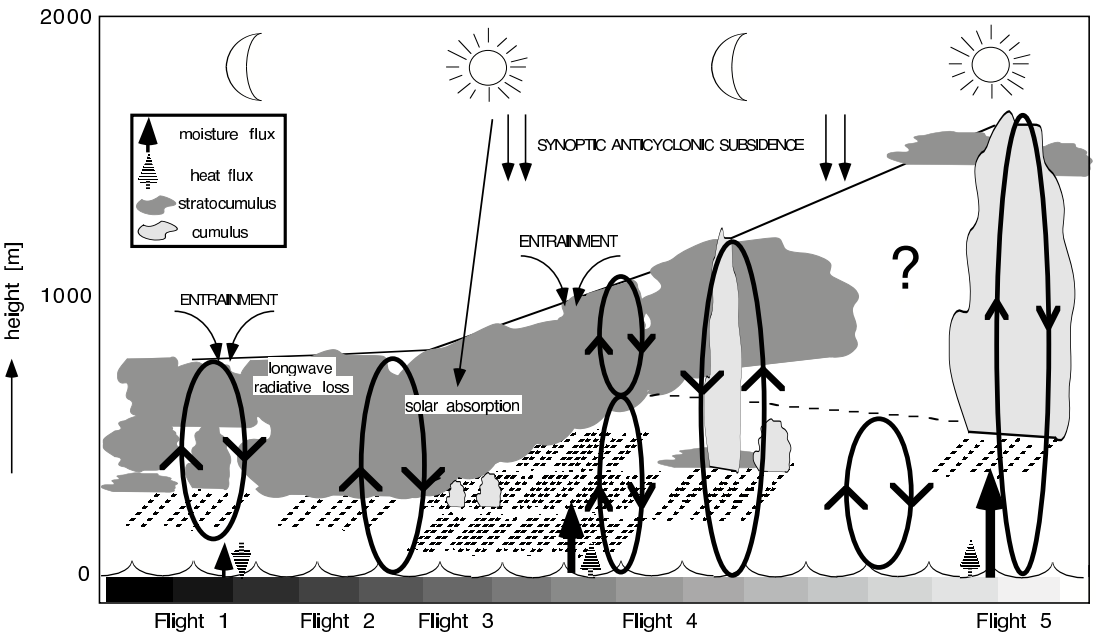

Figure 3.1: A schematic representation of the evolution of the cloudy column of air that was followed during ASTEX. The greyscale bar at the bottom represents the SST as it increases in time. The flight times are indicated at the bottom of the figure (de Roode, 1999).

During flight 1, the cloud layer was not very homogeneous. The cloud layer seemed to consist of two layers. Flights 2 and 3, which took place mainly during nighttime, show a much more homogeneous, well-mixed Sc layer, while during flight 4 the BL shows a clear two layered structure. The Sc layer became gradually thinner and Cu clouds were observed that penetrated this layer. Due to problems with the balloons that were to show the direction of the average wind, it was unclear where the column of air was during the time after flight 4, hence the question mark in the 3.1. An estimated trajectory was used to locate the air mass and flight 5 was undertaken at that position. Judging from satellite pictures, the error made in the estimation of the location is insignificant: the

cloud conditions were homogeneous on a large scale (de Roode, 1999).
During the Lagrangian, the air column was advected equatorwards. Therefore, the SST the air column encountered increased: from approximately 16.8 to 21.1 °C. The result is only a very small increase in sensible heat flux (the grey arrows at the surface) and a strong increase in latent heat flux (the black arrows).
The ASTEX case and the resulting data have been the subject of much research (e.g. Bretherton and Pincus, 1995; Bretherton et al., 1999; Duynkerke et al., 1995; de Roode and Duynkerke, 1997).

3.2 Setup of model intercomparison cases

One of the objectives of ASTEX was to supply modelers with standardized model cases, with well-defined initial and boundary conditions to act as intercomparison cases for modelers. Two of these cases have been described, one based on flight 2 (A209) and the second on flight 3 (RF06). First, a detailed description of the former is given, after which the differences of the second intercomparison case with the first will be discussed. The new model intercomparison case is also based on ASTEX. This time, the entire transition is modelled, starting from flight 2 and ending with flight 5. The results of this case are presented in chapter 5, while the case setup will be presented here.

3.2.1 Intercomparison based on flight A209

This case was originally set up for the 3rd GCSS (GEWEX Cloud System Study) Boundary Layer Cloud Workshop and Fourth International Cloud Modeling Workshop of 12-16 August 1996 [1]. It is based on the data collected by the C-130 aircraft during the second flight of ASTEX. The idealized profiles of q_t and θ_l and of the velocities in the x- and y-directions are as follows:

$$
\begin{array}{r}
0 < z < 662.5 \text{ m} \\
662.5 < z < 712.5 \text{ m} \\
z > 712.5 \text{ m}
\end{array}
\quad
\begin{cases}
\overline{u} = \text{-0.7} & \text{m s}^{-1} \\
\overline{v} = \text{-10.0} & \text{m s}^{-1} \\
\overline{\theta_l} = 288 & \text{K} \\
\overline{q_t} = 10.2 & \text{g kg}^{-1}
\end{cases}
\quad
\begin{cases}
\overline{u} = \text{-0.7 - 0.026(z-662.5)} & \text{m s}^{-1} \\
\overline{v} = \text{-10.0} & \text{m s}^{-1} \\
\overline{\theta_l} = \text{288 + 0.11(z-662.5)} & \text{K} \\
\overline{q_t} = \text{10.2 - 0.022(z-662.5)} & \text{g kg}^{-1}
\end{cases}
\quad
\begin{cases}
\overline{u} = -2 & \text{m s}^{-1} \\
\overline{v} = -10.0 & \text{m s}^{-1} \\
\overline{\theta_l} = 293.5 + 6 \times 10^{-3}(z - 712.5) & \text{K} \\
\overline{q_t} = 9.1 - 2.8 \times 10^{-3}(z - 712.5) & \text{g kg}^{-1}
\end{cases}
\tag{3.1}
$$

Here, u is the velocity in east-west and v the velocity in south-north direction. The overbars denote horizontally averaged values as usual. From these profiles, the initial inversion height is found to be around 687.5 m.

[1] http://www.phys.uu.nl/~wwwimau/old/ASTEX/astexcomp.html

Table 3.2: The forcings of DALES following the case description based on flight A209.

u_g	-2.0	m s^{-1}
v_g	-10.0	m s^{-1}
D	0.5	$\times 10^{-5}$ s^{-1}
$\overline{w'q_t'}\|_0$	0.010	g m kg^{-1} s^{-1}
$\overline{w'\theta_l'}\|_0$	0.010	K m s^{-1}
p_{surf}	1029.0	hPa
z_0	0.2	mm
u_*	0.3	m s^{-1}

The resolution of the used grid is:

$$\mathrm{d}x = \mathrm{d}y = 50 \text{ m}$$
$$\mathrm{d}z = 25 \text{ m}$$

Furthermore, the number of gridboxes is $128 \times 128 \times 64$ giving the total domain a size of $6.4 \times 6.4 \times 1.6$ km^3. This is larger than the domain prescribed in the original case description, however due to parallelization of the code and the use of 32 processors, the mentioned dimensions are more convenient. Since the resolutions are equal and the profiles are averaged in the horizontal directions, the influence on the results is small.
The initial profile of the TKE is:

$$0 < z < 687.5 \text{ m} \qquad \overline{e} = 1 \text{ m}^2\text{s}^{-2}. \tag{3.2}$$

The influence of precipitation is neglected in the description of the case and since the flight took place at night, shortwave radiation is neglected. The only sink term left is the longwave radiative cooling at cloud top. In section 2.3.3 it is described how this effect is taken into account. The radiative jump at cloud top $\mathrm{D}F_R$ derived from measurements is 74 W m^{-2}.

The forcings used in the model case consist of large scale forcings: subsidence and geostrophic wind and of surface forcings: the turbulent fluxes, the surface pressure, the surface roughness z_0 and the friction velocity u_*. This set of surface forcings requires no iterative solving of any variables (Heus et al., 2009). No time dependence of the forcings is assumed. Table 3.2 contains all information on these forcings.
The total simulated time is three hours, of which the first is considered to be the spin-up time of the model.

3.2.2 Intercomparison based on flight RF06

The second intercomparison case is part of the EUropean Cloud REsolving Modelling (EUCREM) model intercomparison project. It was mainly used for comparison between LES and Single Column Models (SCMs). One of these intercomparisons is found in Duynkerke et al. (1999), where results of 4 LES models and 4 SCMs are compared. The article contains the description of the initial conditions and the forcings of the case. On the internet, this case description, together with model results of several models, can also be found [2]. Here, a short description of the case will also be given.

[2] http://www.phys.uu.nl/~wwwimau/old/EUCREM/eucrem.html

The initial profiles are much like those of the first case. The BL is a bit more humid, and the horizontal wind increased slightly:

$$0 < z < 662.5 \text{ m} \quad \begin{cases} \overline{u} &= \text{-1.7} & \text{m s}^{-1} \\ \overline{v} &= \text{-10.0} & \text{m s}^{-1} \\ \overline{\theta_l} &= 288 & \text{K} \\ \overline{q_t} &= 10.7 & \text{g kg}^{-1} \end{cases}$$

$$662.5 < z < 712.5 \text{ m} \quad \begin{cases} \overline{u} &= \text{-1.7 - 0.026(z-662.5)} & \text{m s}^{-1} \\ \overline{v} &= \text{-10.0} & \text{m s}^{-1} \\ \overline{\theta_l} &= \text{288 + 0.11(z-662.5)} & \text{K} \\ \overline{q_t} &= \text{10.7 - 0.032(z-662.5)} & \text{g kg}^{-1} \end{cases}$$

$$z > 712.5 \text{ m} \quad \begin{cases} \overline{u} &= -3 & \text{m s}^{-1} \\ \overline{v} &= -10.0 & \text{m s}^{-1} \\ \overline{\theta_l} &= 293.5 + 6 \times 10^{-3}(z - 712.5) & \text{K} \\ \overline{q_t} &= 9.1 - 2.4 \times 10^{-3}(z - 712.5) & \text{g kg}^{-1} \end{cases}$$

The inversion height is still approximately 687.5 m.
The resolution is also unchanged and the initial TKE is again confined to the BL.

Concerning the forcings there are also no changes. During the flight, the sun started to rise, but it's influence was still small. Therefore, only longwave radiative cooling is modeled, with a flux divergence at cloud top DF_R of 74 W m^{-2}.
There are some prominent changes in the forcings as compared to the first intercomparison case. The surface fluxes have increased, as did the divergence. According to Duynkerke et al. (1999), measurements and the ECMWF model do not show this increase in divergence, but rather a constant value of 0.5 s^{-1}. However, the higher value is chosen to tune to the observed BL thickness in measurements (see equation 2.87). The forcings as prescribed are found in table 3.3.

Table 3.3: The forcings of DALES following the case description based on flight RF06.

u_g	-3.0	m s^{-1}
v_g	-10.0	m s^{-1}
D	1.5	$\times 10^{-5}$ s^{-1}
$\overline{w'q_t'}\big\|_0$	0.018	g m kg^{-1} s^{-1}
$\overline{w'\theta_l'}\big\|_0$	0.013	K m s^{-1}
p_{surf}	1028.8	hPa
z_0	0.2	mm
u_*	0.3	m s^{-1}

3.2.3 New intercomparison based on entire transition

The goal of this project is to describe the transition of a Sc field to a Cu topped BL as it moves in the direction of the equator. Important environmental changes that induce this transitions are increasing SST and decreasing subsidence. This means that the cases, as described above, are not sufficient. Forcings must be made time dependent. In DALESv3.1, options to achieve this are already present. Here, the set up of the

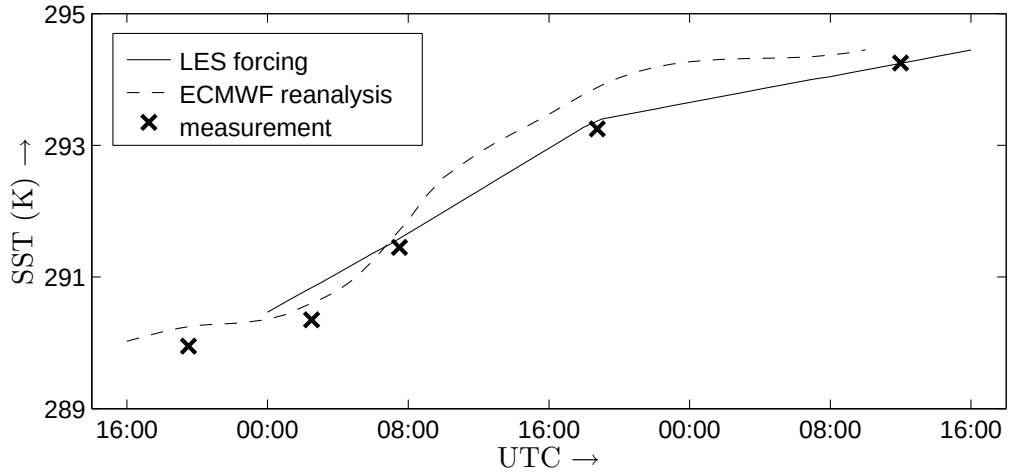

Figure 3.2: The sea surface temperature (SST) in K as a function of UTC time as used in the simulation, as found in the reanalysis using the ECMWF model and as measured during ASTEX. The measurements are averaged values over the duration of flights 1-5. The simulation starts at 0:00 UTC, at the start of flight 2.

transition case will be presented.
The initial conditions as presented in the first section of this chapter are also used in this transition run. This makes flight 2 the starting point. However, in the description of this case, surface fluxes derived from measurements were prescribed. Since measurements of surface fluxes are not available for the entire duration of the experiment, it is more convenient to prescribe the SST. Measurements of the SST are available and can for instance be found in Table 1 of de Roode (1999), where the SST is given in the form of averaged values over the duration of each flight. These values form the basis of the surface forcing. The evolution of the SST as the column of air moves towards the equator is also described by C.S. Bretherton [3], who used the reanalysis data of the ECMWF model to present an intercomparison case for single-column model versions of weather forecast models (Bretherton et al., 1999).
The SST as a function of time as it was implemented into the transition run is given in figure 3.2, as well as the measurements done during the experiment and the reanalysis results. From the surface temperature, DALES uses an iterative procedure to find among others the friction velocity u_* and eventually the surface fluxes (Heus et al., 2009).
The divergence has also been evaluated in the same reanalysis. These values can be found in figure 3.3. Note that the final value of the divergence, $D = 10^{-6}$ s^{-1}, is slightly higher than the value given by Bretherton, $D = -10^{-6}$ s^{-1}. The reason for this is the article by Ciesielski et al. (1999) where divergence is found to be relatively constant and positive for the duration of the first Lagrangian. Anyway, at constant entrainment rate, the difference in divergence causes a difference in inversion height of less than 100 m over 10 hours.
During the measurements, the mean wind changed in direction and in speed. These changes have not been taken into account. Judging from the case descriptions discussed earlier, the change in mean horizontal velocity is only small. However, towards the end of the Lagrangian, measurements show that it decreases quite rapidly to only 3.5 m

[3] www.atmos.washington.edu/~breth/astex/lagr/README.hourly.html

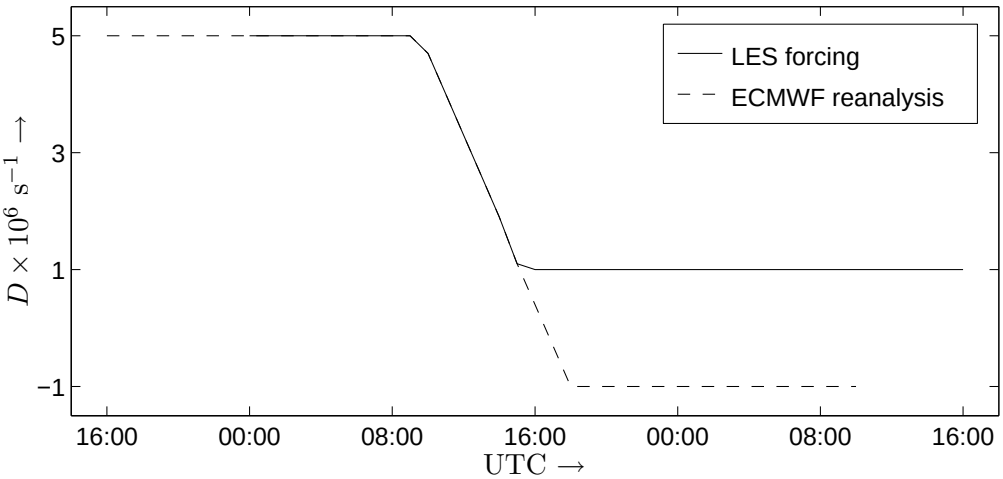

Figure 3.3: The divergence, as used in the simulation and as found in the ECMWF reanalysis, as a function of the UTC time during ASTEX.

s^{-1} during the fifth flight (de Roode, 1999). In STBLs, the effect of wind shear as a TKE producent is usually neglected. It is only significant at the surface and to a lesser extent at the inversion. In this case, however, the SST temperature is prescribed as was already noted. A smaller average horizontal wind velocity means less shear at the surface, resulting in lower turbulent fluxes at the surface. This effect could be quite large. A correct way of implementing the changing wind velocity and direction into the simulation by means of a time dependent geostrophic wind forcing has, during the writing of this thesis, been developed.
Lastly, the effect of radiation is of course also very important. Longwave radiative cooling was lowered slightly to 70 W m^{-2}, as compared to the short intercomparison cases. This time, since the transition spans almost 48 hours, the effect of shortwave radiation cannot be neglected. It is included in a source term as described in section 2.3.3.
The simulated time is 40 hours, starting from 00:00 UTC, which is about 01:00 local time.

Chapter 4

Results model intercomparison cases

The cases described in the previous chapter form a great opportunity to determine the performance of a model. Therefore, DALES also took part in the intercomparison. Both cases were simulated and analysed by Hans Cuijpers, Peter Duynkerke and Margreet van Zanten and the results are gathered, as well as results found by other modellers, on the websites mentioned earlier. Below, the results will be referred to by 'Cuijpers' for convenience.
Some problems with the model became apparent then. For instance, the entrainment rate as diagnosed by the model was the largest of all participants. Since then, much work has been done on the model, in particular by Thijs Heus and Chiel van Heerwaarden. New advection schemes have been included, the time integration method was adjusted and some changes have been made in the cloud top thermodynamics (Stephan de Roode). It is interesting to see what the effect of these adjustments is and whether the model is improved by them or not. Therefore, the intercomparison cases have been simulated, but this time with the most recent model version. The results of this intercomparison are shown in this chapter, starting with the case based on flight A209. Some results of the second case are presented in the next section, while the last section of the chapter deals with the influence of precipitation.
As a check, the results of the MLM are also shown in the results. Unless stated otherwise, the results are averaged over the horizontal plane. Since results of DALES and of the MLM are compared, variables are denoted by the symbol and subscript only, no lines or tildes over the symbols are shown.

4.1 Model intercomparison based on flight A209

Some mean state profiles of both model versions are shown in figure 4.1. Two results obtained by the MLM are shown. To obtain the first results, the diagnosed entrainment from the LES model was used, while the second uses entrainment parametrized by NT. The profiles shown in the figure show a very well-mixed BL. Below the inversion a vertical gradient is hardly found, except in q_t very close to the surface. From the higher inversion and the slightly warmer and dryer BL in the case of Cuijpers, it is clear that the older model entrains much more air into the BL than does DALESv3.1. While the effect on q_t and θ_l does not seem that large, the difference in the profile of the liquid water content

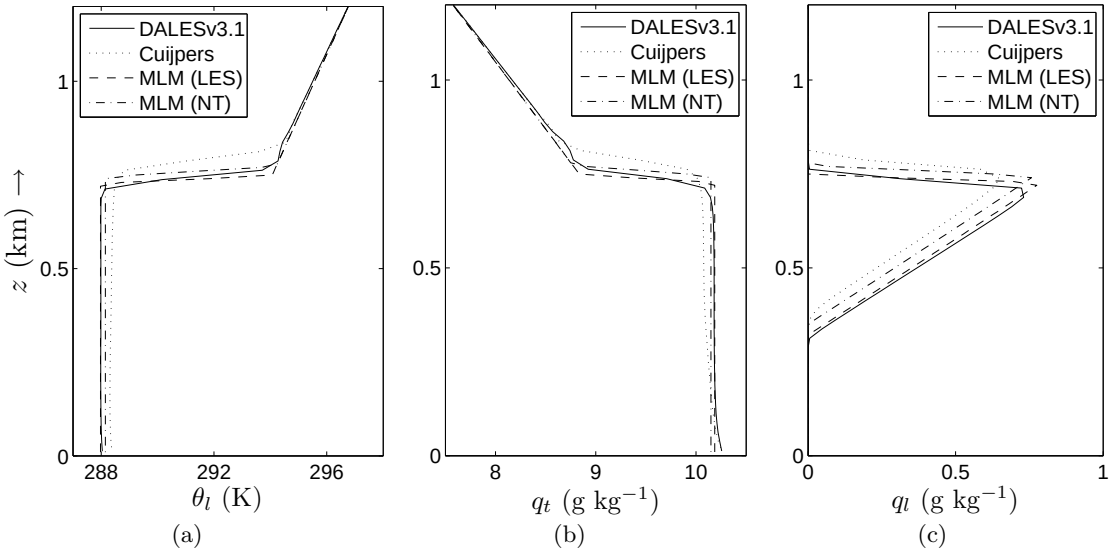

Figure 4.1: Vertical profiles of θ_l (a), of q_t (b) and of q_l (c), averaged over the third hour of simulation. The case description can be found in section 3.2.1. The solid line represents the results of the most recent version of DALES, v3.1, while the dotted line is obtained by Cuijpers using an earlier model version. Results obtained with the MLM are given by the dashed line (entrainment prescribed by the LES model) and the dash-dotted line (entrainment parametrized by NT, $a_2 = 30$).

Table 4.1: LES and MLM results for the intercomparison case based on flight A209 as defined in section 4.1: the diagnosed/parametrized entrainment w_e and the liquid water path W, averaged over the third hour of the simulation. The MLM in which the entrainment rate is prescribed, uses the value found by DALESv3.1, instead of actually diagnosing it.

setup	w_e (cm s^{-1})	W (g m^{-2})
Cuijpers	1.44	177
DALESv3.1	1.04	202
MLM (entr. by LES)	-	198
MLM (entr. by NT)	1.13	191

is obvious. The maximum value of q_l is lower while cloud base height is higher in the case of Cuijpers. This will lead to a lower LWP, even though the inversion is also higher. In this intercomparison, it is striking how well the MLM performs. In combination with the entrainment from the LES model, the results are almost indistinguishable from those of DALESv3.1. The parametrisation overestimates the entrainment rate a bit, but it is still much closer to DALESv3.1 than the older model.

The average entrainment rates and the LWP as found by the different models are located in table 4.1. From this table it becomes apparent how large the difference in entrainment rate actually is: that found by Cuijpers is almost 40% higher than in the most recent model, while the MLM is less than 10% off. The difference in LWP is smaller, but in the case of Cuijpers still more than 10%. That this difference is smaller can be explained by the fact that entrainment has two effects on the LWP. On the one hand, entrainment causes evaporation of liquid water from the cloud, decreasing the LWP, while on the other hand, the BL deepens and cloud top height increases. If the increase in cloud top height is larger than that in cloud base height, the latter effect increases the LWP, since

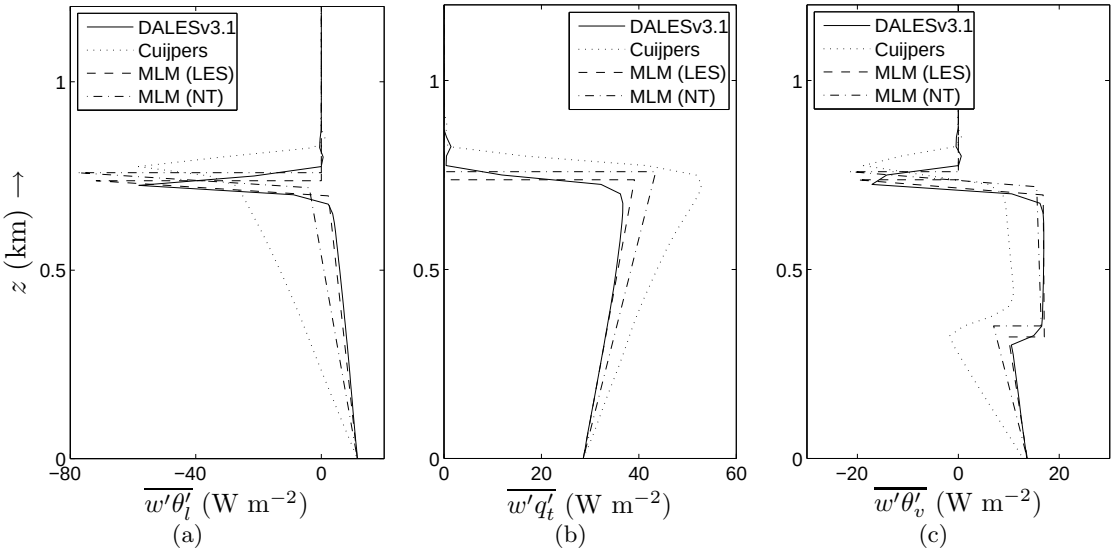

Figure 4.2: Vertical profiles of the total (filtered + SFS) turbulent fluxes $\overline{w'\theta_l}$ (a), $\overline{w'q_t'}$ (b) and $\overline{w'\theta_v'}$ (c), averaged over the third hour of simulation. The case description can be found in section 3.2.1. Legend as in figure 4.1.

it is the integral of q_l over height.
The turbulent structure of the BL as found by the models is shown in figure 4.2.
In the light of the discussion above, the results in this figure are not surprising. The conserved variable fluxes are, in a well-mixed BL completely determined by the surface fluxes and the fluxes at the BL top, which are a function of the entrainment rate and the jump of the variable. Assuming the inversion jump is roughly equal in all models, the entrainment controls what the profiles look like. A large entrainment rate causes $\overline{w'\theta_l'}$ to have a more negative slope, while the flux of q_t gets a more positive slope. Again, the MLM with LES entrainment represents the results of DALES very well.
The flux of θ_v, shown in figure 4.2(c), has some interesting features. For instance, where the MLM shows an actual jump in buoyancy at cloud bottom, which signifies the change from the use of dry coefficients to saturated ones, DALES shows a more gradual change. This difference is caused by the averaging in the horizontal directions. The minimum buoyancy flux below cloud bottom is therefore always smaller in the case of the MLM. This minimum is also clearly affected by the entrainment rate. This is also apparent from the figure. The model with the highest entrainment rate, that of Cuijpers, even shows an area with negative buoyancy flux at cloud bottom. This negative buoyancy flux has a direct link to decoupling, which becomes obvious by looking at the prognostic equation for the mean vertical velocity variance (see e.g. Stull, 1993):

$$\frac{\partial \overline{w'^2}}{\partial t} = 2\frac{g}{\theta_0}\overline{w'\theta_v'} - 2\overline{w'\frac{\partial \pi'}{\partial z}} - \frac{\partial \overline{w'^3}}{\partial z} - \varepsilon_{w'^2}, \tag{4.1}$$

in which the last term on the rhs is the dissipation rate of $\overline{w'^2}$ and terms involving mean velocities are zero. All variables in this equation denote the filtered part. The only production term in this equation is the first term on the rhs: the term involving the turbulent flux of $\overline{w'\theta_v'}$. A negative buoyancy flux therefore decreases $\overline{w'^2}$, which is the vertical component of the TKE, since the TKE is defined as the sum of the mean

velocity variances in the $x-$, $y-$ and $z-$directions. This effect is also visible in the plot of the vertical velocity variance, shown in figure 4.3.

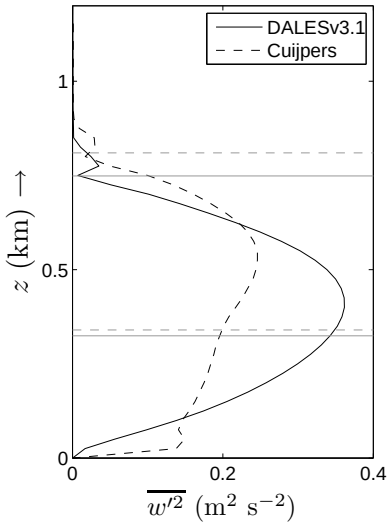

Figure 4.3: Vertical profiles of the filtered vertical velocity variance $\overline{w'^2}$, averaged over the third hour of the simulation. The case description can be found in section 4.1. The solid line represents the results of the most recent version of DALES, v3.1, while the dashed line represents the results obtained by Cuijpers, using an earlier version of DALES. The grey lines represent cloud base and cloud top for both models.

The profile from DALESv3.1 is a very smooth line with a single peak, approximately in the middle of the BL, while the older model finds a dip around cloud bottom, where the buoyancy flux was observed to be negative.
The dip observed is not very strong, but when $\overline{w'\theta_v'}$ stays negative, a minimum vertical velocity variance is expected to form at cloud bottom. When this is the case, the BL is more or less split in two layers, a cloud layer and a subcloud layer. The smaller the value at the minimum of $\overline{w'^2}$, the less turbulent transport there is between the two. This is the process of decoupling.
In light of this discussion, it is logical to develop a decoupling criterion based on the buoyancy flux. Turton and Nicholls (1987) introduced the buoyancy integral ratio, BIR:

$$\mathrm{BIR} = -\int\limits_{\substack{\overline{w'\theta_v'}<0 \\ z<z_b}} \overline{w'\theta_v'}\,\mathrm{d}z \Bigg/ \int\limits_{\text{other } z} \overline{w'\theta_v'}\,\mathrm{d}z. \tag{4.2}$$

The limit for a well-mixed layer was initially set to 0.4. However, according to Bretherton and Wyant (1997) a lower value is more appropriate since well-mixed BLs with BIR values exceeding 0.15 have not been found in measurements nor in simulations. For the simulation done by Cuijpers, BIR is only small, approximately 0.01.

4.2 Model intercomparison based on flight RF06

For the second intercomparison case, that is based on flight RF06, the mean state results show roughly the same picture as those of the first intercomparison case (figure 4.1). The BL, as simulated by DALESv3.1, is very well-mixed, except for q_t very close to the

surface. The effect is somewhat stronger than in A209 because of the higher surface flux of q_t. The model results of Cuijpers however, show clearly two layers in both θ_l and q_t. The effect is that the liquid water content is much smaller. This is also clearly visible in table 4.2, where the entrainment rate and the LWP are given for the different models.

Table 4.2: LES and MLM results for the intercomparison case based on flight RF06 as defined in section 3.2.2: entrainment w_e and liquid water path W, averaged over the third hour of the simulation. The MLM in which the entrainment rate is prescribed, uses the value found by DALESv3.1, instead of actually diagnosing it.

Model	w_e (cm s^{-1})	W (g m^{-2})
Cuijpers	2.02	139
DALESv3.1	1.69	211
MLM (entr. by LES)	-	210
MLM (entr. by NT)	1.55	203

The difference between the two LES models is striking: the older model has one third less liquid water than the most recent version. In this case, the entrainment rates differ not that much, about 15%. Again, the MLM is very much like the DALESv3.1. In the case of prescribed entrainment, the LWP is unlikely close, while that in the case of parametrized entrainment is only a few percent off. The parametrized entrainment is also very close, being less than 10% off.

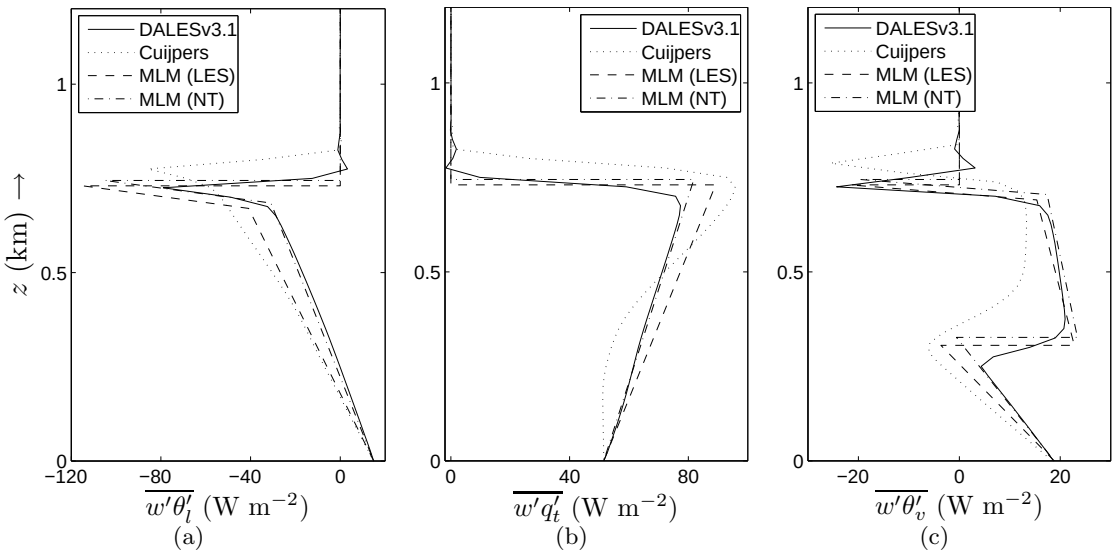

Figure 4.4: Vertical profiles of the total (filtered + SFS) turbulent fluxes $\overline{w'\theta_l}$ (a), $\overline{w'q_t'}$ (b) and $\overline{w'\theta_v'}$ (c), averaged over the third hour of simulation. The case description can be found in section 3.2.2 and the legend is as in figure 4.1. Note that the axis are *not* equal to those in figure 4.2.

Plots of the turbulent flux profiles found by the models are shown in figure 4.4. It is clear from the profiles that the model of Cuijpers does not result in a well-mixed BL: especially the $\overline{w'q_t'}$ profile is not linear anymore.
The BL found by DALESv3.1, on the contrary, *is* well-mixed and is still represented quite well by the MLM. Surprisingly, the smaller parametrized entrainment results in profiles

that agree better with DALES than do the profiles based on the actual entrainment rate. The reason for this is unclear, but it seems that the mean vertical profiles found by DALES are also not entirely linear. Possibly, decoupling is already influencing some parts of the domain in a way that also effects the turbulent fluxes.
Judging from the buoyancy fluxes in figure 4.4(c), the BL is not far from decoupling. The model of Cuijpers again results in negative buoyancy fluxes below cloud base, this time corresponding to a BIR value of 0.11. The MLMs also give negative buoyancy fluxes, although their BIR values are much smaller: 0.01 for the LES entrainment and practically 0 for the parametrized entrainment.
It was already noted that the averaged LES profiles show marks of inhomogeneity at cloud base. Here a problem is encountered in that respect: the MLM profiles result in negative buoyancy fluxes far earlier than the averaged LES profiles do. This leads to a bias in the BIR values found by the MLM.

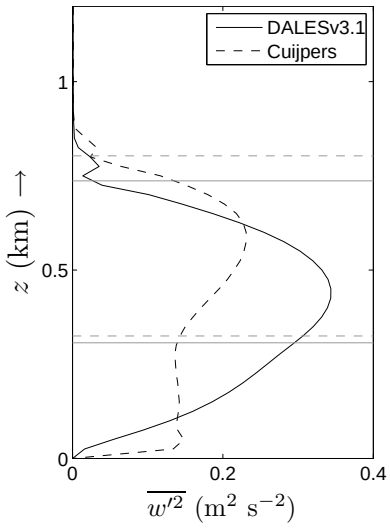

Figure 4.5: Vertical profiles of the filtered vertical velocity variance $\overline{w'^2}$, averaged over the third hour of the simulation. The case description can be found in section 3.2.2 and the legend is equal to that of figure 4.3.

The profiles of the vertical velocity variance, in figure 4.5, are in agreement with the buoyancy profiles: near the levels where Cuijpers' model results exhibit negative buoyancy fluxes, there is a weak local minimum in $\overline{w'^2}$. On the other hand, DALESv3.1 still gives a single peaked structure and thus a well-mixed BL.

4.3 Influence of precipitation

In the introduction of this thesis, it was already mentioned that the precipitation might have an effect on the dynamics and especially on the decoupling of the BL. For a long time however, the effect has been neglected due to lack of computational power required to model the complex processes involved with microphysics. The intercomparison cases as they are presented in the previous section also do not include this effect. Since DALES has two bulk microphysics schemes implemented, it is interesting to see what the effect on the dynamics of the BL is.
Figure 4.6 shows vertical profiles of the precipitation rate, averaged over the third hour. Two other profiles are included in this plot. The dashed line represents the result

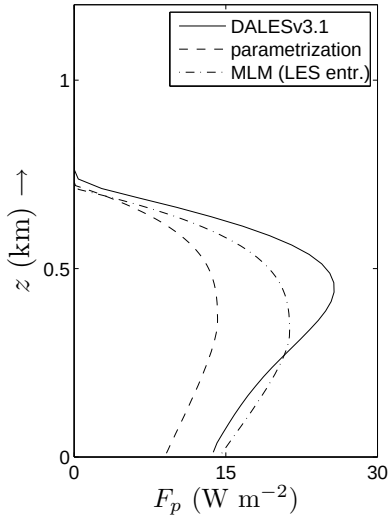

Figure 4.6: The precipitation rate as a function of height as resolved by the LES model (solid line), as found using the parametrization of equation (2.102) (dashed line) and as found using this parametrization in the MLM (dash-dotted line).

of the parametrization given in equation (2.102) in which the mean LWP, z_b and z_i from the LES are used. The second profile (dash-dotted line) gives the result of the parametrization when the mean MLM values are used.
It is clear that the parametrization results in less precipitation than does the KK scheme used in DALES. The maximum value is almost a factor two smaller. However, when the parametrization is used in the MLM, the precipitation rate confirms much better with the DALES. This is mainly due to the larger LWP and the higher cloud bottom as found by the MLM.
The liquid water that leaves the BL at the surface is the only direct effect precipitation has on the mean state variables. As already mentioned in section 2.4.3, due to this flux, the BL becomes dryer. From figure 4.6 it is obvious that the flux is small: only about 15 W m^{-2} as compared to radiative cooling (74 W m^{-2}) and the surface latent heat flux (50 W m^{-2}). Turbulent fluxes at the top are even larger than the mentioned values, therefore, the error made in neglecting precipitation seems to be acceptable for the mean state of the BL. However, including microphysics appears to have a significant effect on the turbulence structure of the BL.

Table 4.3: LES and MLM results for the intercomparison case based on flight RF06 as defined in section 3.2.2, including microphysical effects: entrainment rate w_e, liquid water path W and buoyancy integral ratio BIR, averaged over the third hour of the simulation.

Model	w_e (cm s^{-1})	W (g m^{-2})	BIR -
DALESv3.1	1.59	140.6	0.040
MLM (entr. by LES)	-	177.5	0.043
MLM (entr. by NT)	1.60	165.6	0.127

In table 4.3, the entrainment rate, the liquid water path and the BIR value can be found for the LES run including precipitation. The effect of microphysics causes a small difference in the entrainment rate of a few percent. The liquid water path, however,

has decreased by almost a third. Furthermore, the BIR value is not zero anymore. The dynamics inside the BL must have changed significantly. The conserved variable flux profiles (figure 4.7) indeed show this difference.

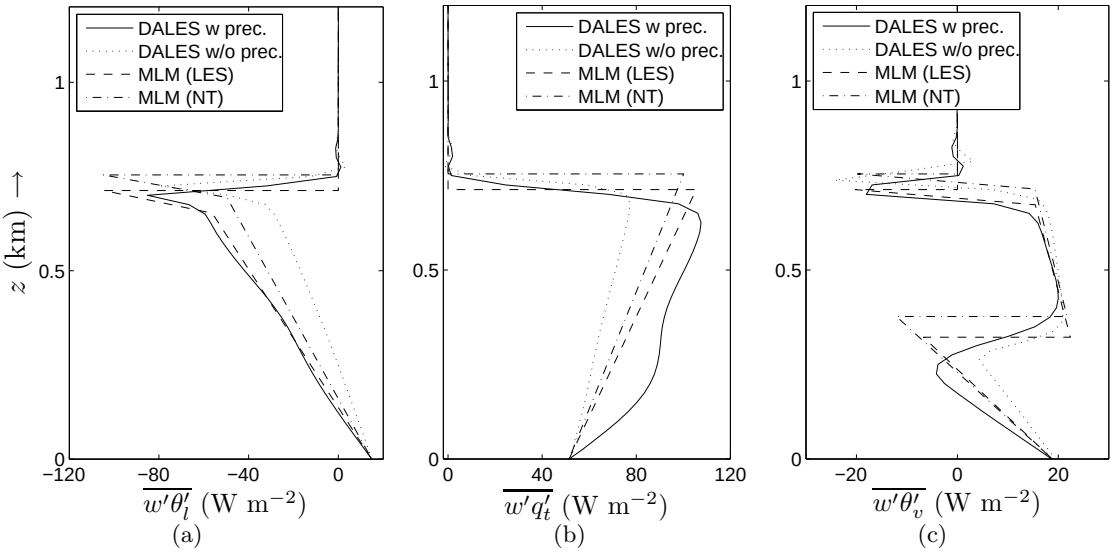

Figure 4.7: Vertical profiles of the total (filtered + SFS) turbulent fluxes $\overline{w'\theta_l}$ (a), $\overline{w'q_t'}$ (b) and $\overline{w'\theta_v'}$ (c), averaged over the third hour of simulation. The case description can be found in section 3.2.2. The solid line represents the result from DALESv3.1 including precipitation, while the results without precipitation are given by the dotted line as a comparison. The dashed and the dash-dotted line show the results of the MLM with LES entrainment and precipitation and the stand-alone MLM respectively.

It should be noted that in the LES model, a separation is made between cloud water (small droplets) and rain water (droplets with radii larger than 50 μm). This means that the rain water flux is not included in the 'total' water flux. Therefore, the surface flux of $\overline{w'q_t'}$ has not changed. Also due to this separation, a part of q_t is constantly removed inside the cloud layer. To maintain a well-mixed layer, the turbulent flux needs to increase. This is the effect observed in the cloud layer.
Below the cloud layer, part of the rain water evaporates. Again, the turbulent flux adopts in order to keep the layer well-mixed. This causes the higher humidity flux in the subcloud layer.
To include the effect of precipitation into the flux profiles of the MLM, the precipitation rate as a function of height can be included in equation (2.108). Here however, the maximum precipitation flux is simply added to $\overline{w'q_t'}$ and subtracted from $\overline{w'\theta_l'}$ at the top of the BL. As shown in figure 4.7, this is a very good approximation for $\overline{w'\theta_l'}$, while the total humidity flux is slightly underestimated, especially below cloud base. In this figure, The dashed line is found from the MLM using the entrainment rate and the precipitation profile of the LES model, while the dash-dotted line is the MLM in which entrainment and precipitation are parametrized.
The buoyancy flux of figure 4.7(c) also shows good agreement, although the stand-alone MLM has a relatively high cloud base, resulting in a larger area of negative buoyancy flux. The BIR value is, therefore, also overestimated.
Here, a great advantage of the parametrization of NT becomes clear. Because it uses the buoyancy flux (in the absence of entrainment) to calculate the entrainment rate, the

effect of precipitation is easily included.
Finally, figure 4.8 shows the profiles of the vertical velocity variance of the simulation with microphysics (solid line) and that without (dotted line).

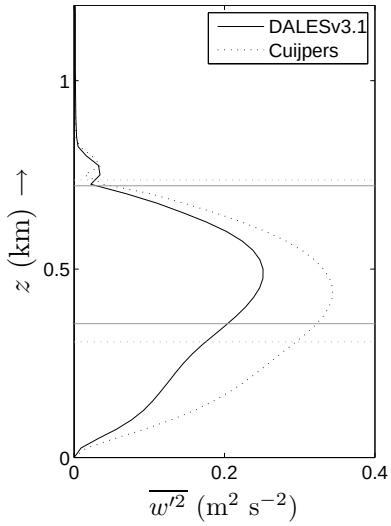

Figure 4.8: Vertical profiles of the filtered vertical velocity variance $\overline{w'^2}$, averaged over the third hour of the simulation. The case description can be found in section 3.2.2 and the legend is equal to that of figure 4.3.

The negative buoyancy flux below the cloud layer causes $\overline{w'^2}$ to be smaller overall. Furthermore, the maximum value lies a bit higher up in the BL. The change caused by the inclusion of microphysics into the models is striking and shows that neglecting precipitation leads to better mixed layers, which may not be a good representation of the actual situation. Therefore, microphysics are included in the new intercomparison case, that is presented in the following chapter.

Chapter 5

LES and MLM results of the ASTEX Sc to Cu transition

In this chapter, the LES results of the intercomparison case based on the Sc to Cu transition as observed during ASTEX, are presented. The description of this case can be found in section 3.2.3. First of all, the mean state results from DALESv3.1 are shown and compared to data gathered during the flights of the first Lagrangian of ASTEX. The same is done with vertical profiles concerning the turbulent fluxes of moisture and heat in the BL.
In the last section of this chapter, the MLM results are compared to the results obtained by DALES, to find an answer as to whether or not the MLM can be used to do predictions on BL decoupling and cloud break-up during the transition.

5.1 Mean state

The results of the simulation show clearly a part of the transition. During the first 30 hours, the simulated Sc layer has a cloud cover of 1. After this time, which is at 6:00 UTC, the average cloud cover starts to drop and patches of clear sky can be found. The timing is interesting here. The strong warming effect of shortwave radiation has been absent over a period of ten hours or so and is still weak at this time. The fact that at that moment a clear sign of cloud dissolving is observed, means that the during the night another process was responsible for break up of the cloud layer. That the responsible process is most likely decoupling, resulting in the drying of the cloud layer, will be shown in the remainder of this chapter.
Figure 5.1 contains hourly averaged profiles of the total humidity around the times of the flights. The measurements done during these flights are also included. It is striking how well the LES results and the measurements, especially during flights 3 and 4, agree. During flight 2, DALES predicts a slightly larger gradient in q_t and θ_l in the BL than the measurements show. The simulated BL is therefore less well-mixed than in the measurements. Furthermore, during flight 5, the difference between model results and measurements is relatively large in the lower BL. It seems that the surface flux of q_t is overestimated by DALES. The intercomparison cases based on flight 2 and 3 prescribe values of $\overline{w'q_t'}$ at the surface of 0.01 and 0.013 g m kg^{-1} s^{-1} respectively, while the modeled surface fluxes are much larger: 0.018 and 0.023 g m kg^{-1} s^{-1}, almost a factor of 2 larger.

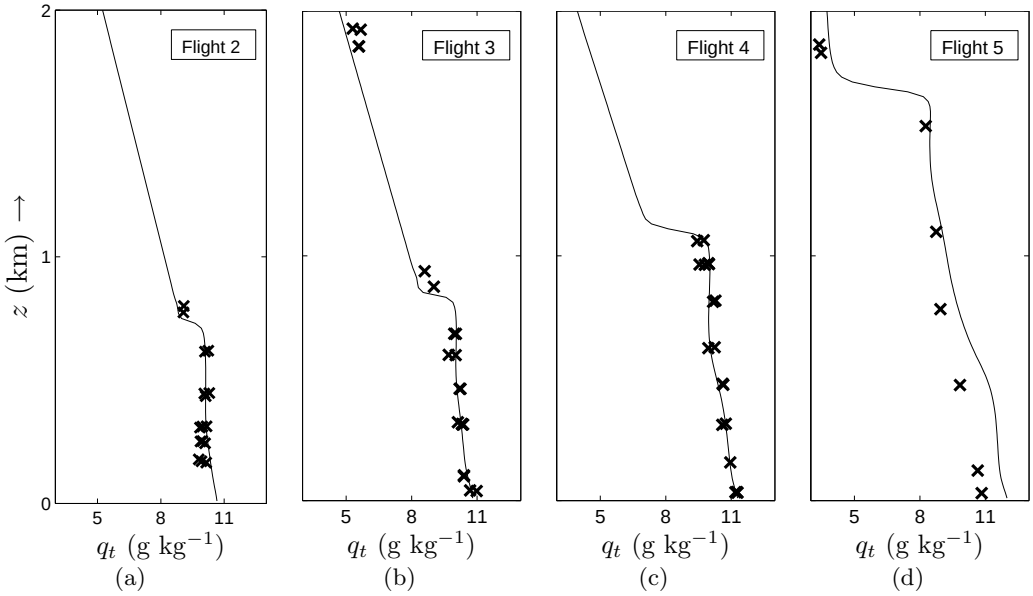

Figure 5.1: Hourly averaged profiles of q_t of the 3rd (a), 8th (b), 19th (c) and the 36th hour (d) plotted with the measurement data as found during the five ASTEX flights.

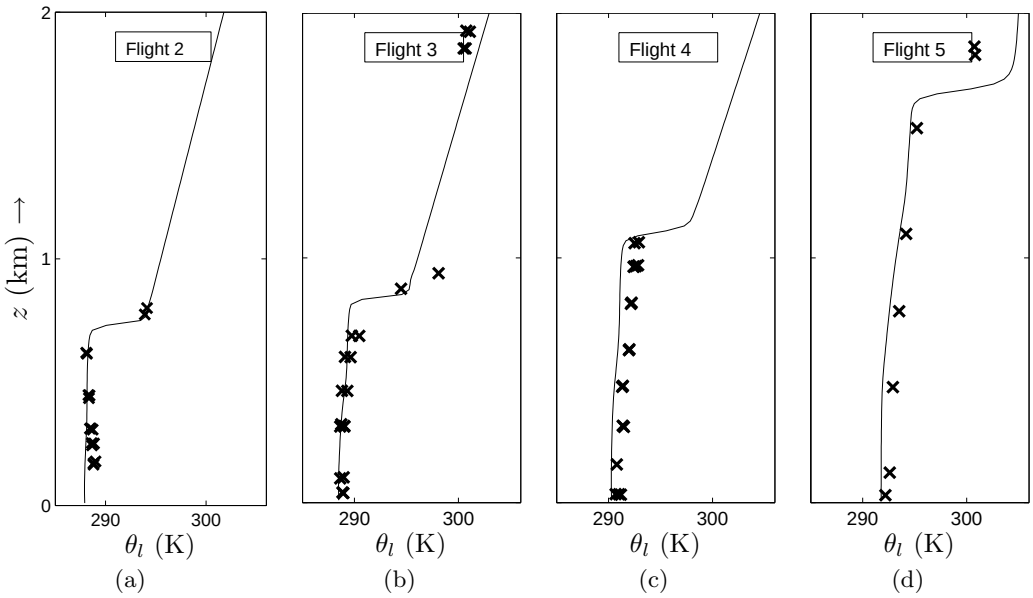

Figure 5.2: Hourly averaged profiles of θ_l of the 3rd (a), 8th (b), 19th (c) and the 36th hour (d) plotted with the measurement data as found during the five ASTEX flights.

Profiles of θ_l during the transition can be found in figure 5.2. Again, measurements and model results agree very well. During flights 4 and 5, the predicted BL is slightly cooler than the actual one, but the difference is never very large. Again, the surface fluxes seem to be causing the difference. For $\overline{w'\theta_l'}$ however, the modeled surface fluxes are *smaller*: only 60% of the values given in the case descriptions.

A solution to the problem is not very obvious. In the description of this simulation, in section 3.2.3, it was mentioned that the prescribed wind velocity is too high in the second

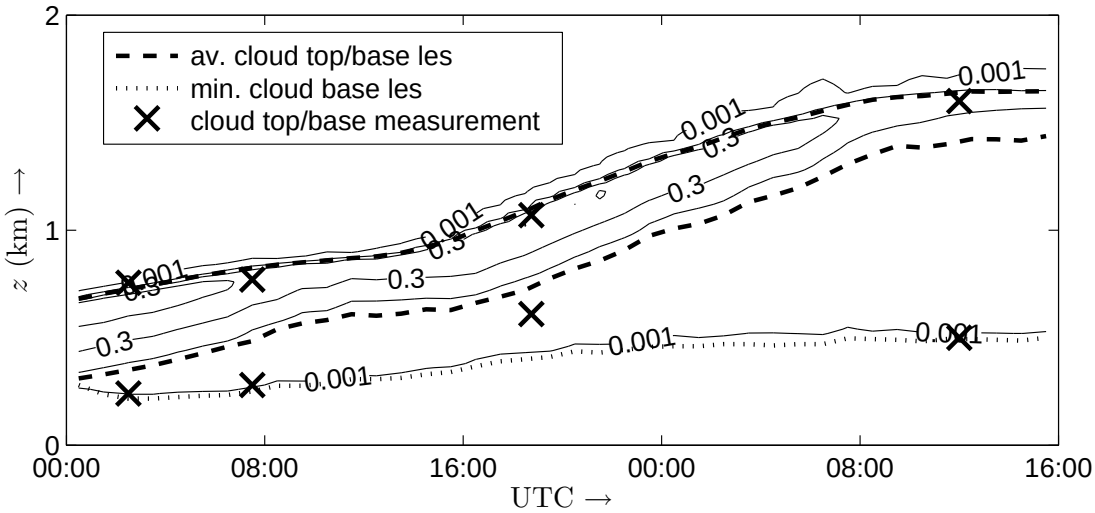

Figure 5.3: A contourplot of the liquid water content, q_l, diagnosed by DALESv3.1 as a function of height and UTC time, with contours at 0.001, 0.1, 0.3 and 0.5 g kg^{-1}. The thick dashed lines represent the horizontally averaged cloud top and base, while the dotted line is the minimum cloud base in the domain. The crosses represent the measured cloud top and base height during ASTEX.

half of the run. This explains the large difference in q_t during flight 5. However, reducing the wind velocity will also mean a smaller flux of θ_l, which was already too small. A time dependent forcing of the wind speed will therefore not be the entire solution to this problem.

Figure 5.3 shows the entire transition in the form of a contourplot of q_l, the liquid water content. From the beginning of the simulation the bulk of the Sc layer starts to rise and decrease in thickness, while the minimum height at which liquid water can still be found stays virtually constant.

The model results fit the measurements extremely well. Cloud top is overestimated a bit, but the difference is only small. Cloud base measurements are in good agreement with the minimum cloud base in the LES model. During the fourth flight (third in the figure), the difference between measurement and LES is largest. It is unclear what causes this difference. It could be that the effect of shortwave radiation in the model is somehow underestimated, leading to less evaporation of cloud liquid water and a lower cloud base. This is, however, not very likely, since cloud base in the last measurement is again in very good agreement with the LES result.

It is more likely that the difference is caused by the inhomogeneous character of clouds below the Sc layer, which is also apparent in the contour plot. The area in between average and minimum cloud base has a very low average liquid water content, likely caused by patchy Cu cloud formations. Therefore, cloud base varies a lot in the horizontal directions, making measurements very dependent on location.

The decreasing cloud liquid water contents in the BL results in a LWP that is also decreasing with time. The evolution of the LWP is presented in figure 5.9 in section 5.3. Here, two contourplots of the horizontal distribution of the LWP are shown (figure 5.4). These plots show how the cloud develops from a thick, relatively homogeneous, layer into a thinner layer, with some very sharp peaks in LWP, reflecting the presences of cumuli.

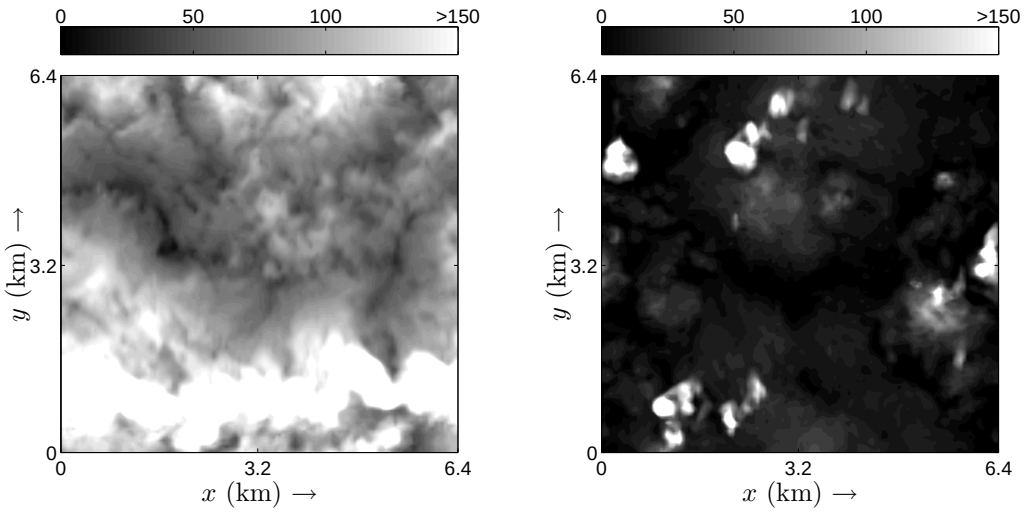

Figure 5.4: Contourplot of the LWP in the horizontal directions. The plots show the instantaneous distribution of the LWP after 8 hours (a) and after 40 hours of simulated time. The area averaged LWPs are 104 and 24 g m^{-2} respectively.

The mean LWP decreases by about 75% over a period of 32 hours, while the maximum value found in the domain *increases* by 50%, from 380 to 610 g m^{-2} (instantaneous values). This indicates that the BL becomes less homogeneous in the horizontal directions. Strong thermals from the surface results in Cu-like structures, with a very high LWP.

5.2 Turbulence structure of the BL

The mean state profiles show that the BL starts out quite well-mixed, but becomes more and more decoupled towards the end of the simulation. As in the previous chapter, this change should also be visible in the flux profiles and especially in the buoyancy flux profiles. Figure 5.5(a) shows this flux as a function of time in the form of a contourplot. This plot shows some interesting features. First of all, there is an obvious diurnal cycle visible. During the afternoon and the night, when shortwave radiation is present, the buoyancy flux is highest, while around noon, it is much smaller. This shows again that surface fluxes are not the driving force behind the turbulence in the BL. If this were the case, the warming effect of the sun on the surface would increase the buoyancy at the surface and thus also the turbulence. In a STBL, longwave radiative cooling is the driving force and during the day this cooling is partially or entirely offset by the warming effect of the absorption of shortwave radiation. Therefore, during the day hardly any buoyancy is created at the BL top.

Another interesting point, which is also expected, is that the maximum buoyancy is confined to the Sc cloud layer, between the mean cloud base and top height. This is caused by the warming effect of the condensation of water vapor, that rises from the surface. Towards the end of the simulation, Cu clouds increasingly form around minimum cloud base height, causing extra buoyancy below the Sc layer. This eventually results in the smooth profile shown in figure 5.5(e).

Also, a fact that clearly shows the decoupling of the BL is the average cloud base, which

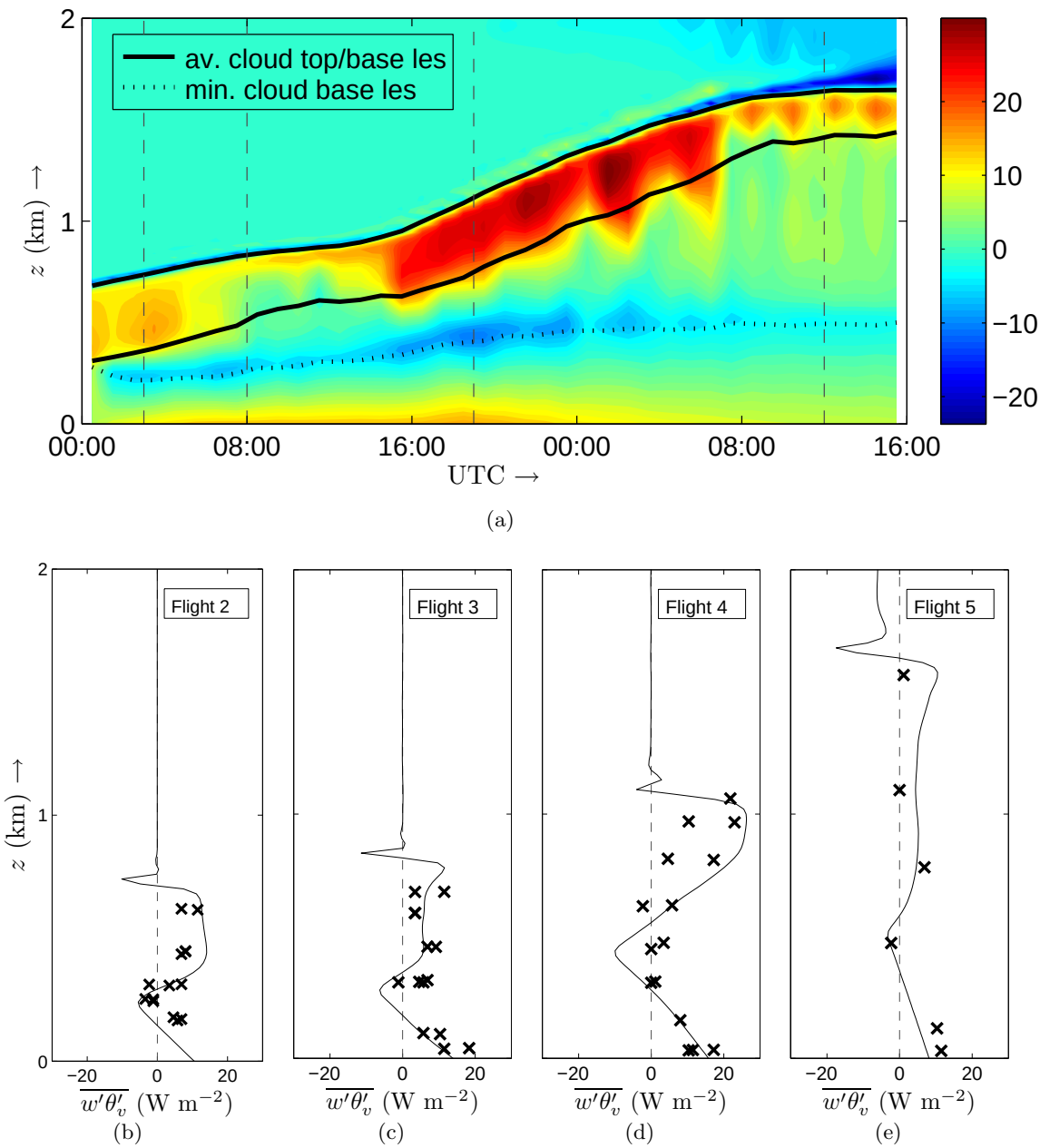

Figure 5.5: A contourplot of the turbulent flux of θ_v in W m^{-2} (hourly averaged) as a function of height and UTC (a). The vertical dashed lines represent the hours at which the vertical profiles are plotted against the measurements made during the ASTEX flights 2 (b), 3 (c), 4 (d) and flight 5 (e).

has a different height than the level of the minimum buoyancy flux, indicated in the contourplot by the light blue area around the lowest cloud base.

Figures 5.5(b)-5.5(e) show hourly averaged profiles of $\overline{w'\theta_v'}$ at approximately the times the ASTEX flights were conducted. The model results show a reasonable resemblance to the measurements. Inside the cloud however, the model results are always relatively high compared to the observations. At the surface, the effect of the low θ_l flux found by DALES is obvious. In unsaturated situations, this flux is the major constituent of the

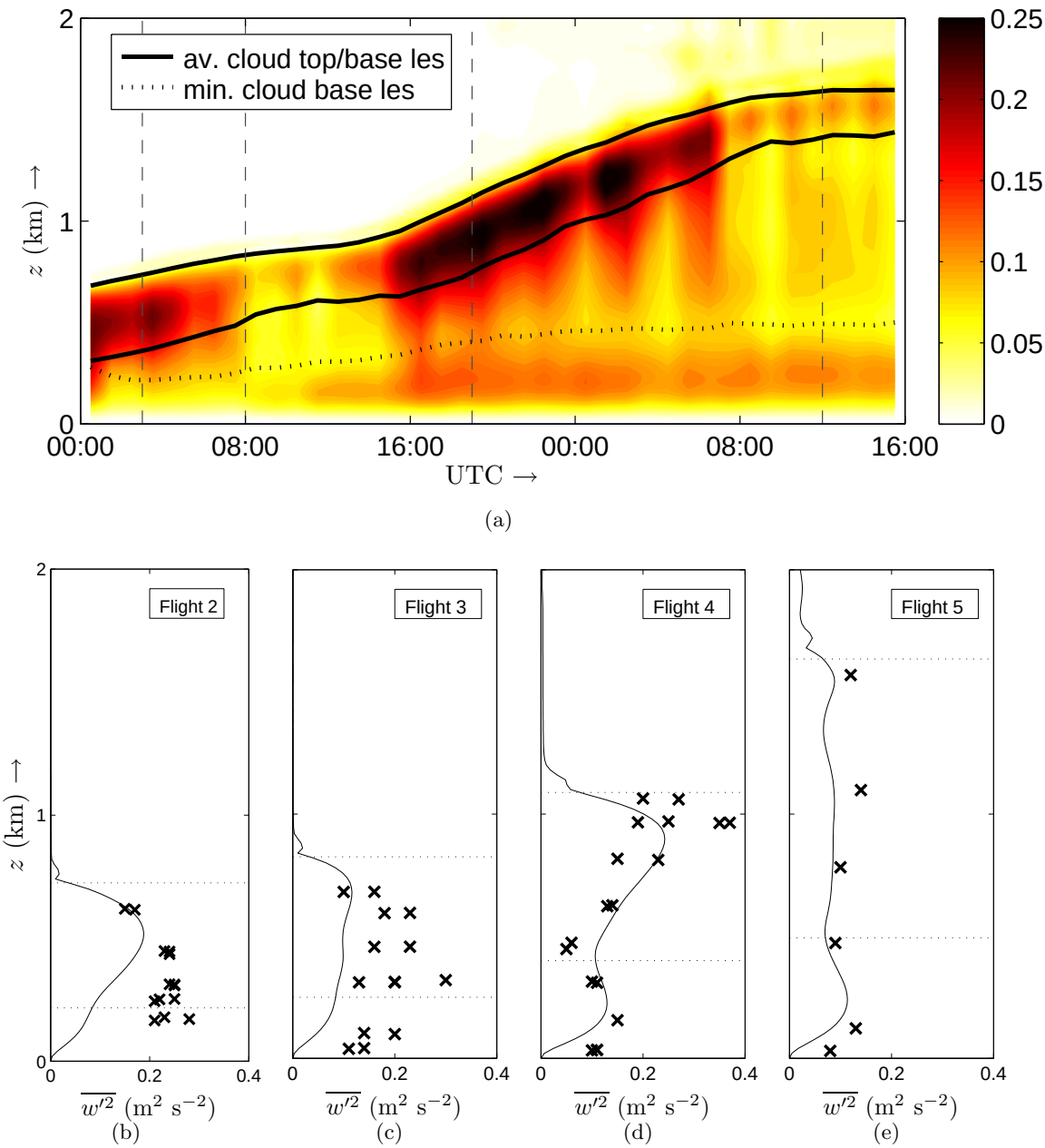

Figure 5.6: A contourplot of the (hourly averaged) resolved vertical velocity variance in m^2 s^{-2} as a function of height and UTC (a). The vertical dashed lines represent the hours at which the vertical profiles are plotted against the measurements made during the ASTEX flights 2 (b), 3 (c), 4 (d) and flight 5 (e).

buoyancy flux. In most flights, the modeled $\overline{w'\theta_v'}$ at the surface is too small.
Above the BL in figure 5.5(e), strange behaviour is observed. This is a the results of a wrong prescription of the change in the geostrophic wind over time, resulting in too much shear above the BL. It is obvious from the contour plot that this only affects the top of the very last part of the BL.
What is most important here, is that both measurements and DALES show significantly negative buoyancy fluxes below cloud base. As found in the previous chapter, this must

also show in the profiles of the negative velocity variance. These profiles are shown in figure 5.6, as well as a contourplot of $\overline{w'^2}$ over the entire simulation. This plot also shows clearly the diurnal cycle, with large values during the afternoon and the night and smaller ones around noon. The decoupling of the BL is also clearly seen. It is obviously an evolving process: during the morning of the first day, between flight 2 and 3, decoupling is hardly observed. Around noon two peaks can already be distinguished and during flight 4 the BL is clearly decoupled in both the simulation and the measurements. Even during the night, the BL stays decoupled. It is therefore a typical case of deepening-warming decoupling, in contrast to decoupling induced by shortwave radiation. Solar radiation is know to cause decoupling, but this decoupling will show a diurnal cycle with a better mixed BL during the night. Deepening-warming decoupling includes the idea that deeper BLs tend to be more decoupled (Bretherton and Wyant, 1997), caused by an increased latent heat flux at the surface. This form of decoupling can start at night and has a more irreversible character.
Regarding the measurements, it is obvious that the model underestimates the vertical velocity variance. Especially during flights 2 and 3 (figures 5.6(b) and 5.6(c)) the difference is large, up to a factor of 2. A possible explanation could again be the underestimation of $\overline{w'\theta_l'}$ at the surface, with leads to the overestimation of the negative buoyancy flux below cloud base. Furthermore, in the previous chapter, it was observed that precipitation causes $\overline{w'^2}$ to decrease dramatically, also leading to a smaller vertical velocity variance. Overestimation of the precipitation rate can also lead to the difference.
Overall, it is clear that the BL decouples quite rapidly. The BIR value however, which is shown for the transition in figure 5.7, does not show an increase as the BL decouples. It has a maximum at around 8:00 UTC (twice) and decreases towards a minimum at night. From the profiles of $\overline{w'^2}$ it is clear that the BL gets more and more decoupled. This shows that the value of BIR gives a tendency towards decoupling, instead of the instantaneous decoupling. Stevens (2000) arrived at a similar conclusion. In a series of LES simulations, in which BIR was a control parameter, signs of a two-layered structure were found for BIR > 0.10. Stevens' conclusion was that a BL is unable to stay well-mixed for BIR > 0.

5.3 Comparison of MLM to LES results of the transition

Above, it was observed that the BL became more and more decoupled during the transition. Decoupling causes the assumption of well-mixedness not to apply anymore. Therefore the MLM is expected to fail further into transition. Still it is interesting to compare the model results to those of DALES. This can be done in two ways: 1) Compare the LES results to a MLM with prescribed entrainment rates, surface fluxes and precipitation from the LES model and 2) compare the LES results with a stand-alone MLM.
The first option gives the opportunity to study decoupling to find the moment at which the mixed-layer assumption fails. This would be the moment that both models start to diverge. The second possibility can be used to see how well the MLM performs and whether or not it can used to replace the LES model. A clear view of the conditions in which the MLM can be used, makes sensitivity studies with it possible.

5.3.1 MLM with prescribed entrainment, surface flux and precipitation

Figure 5.8 shows the evolution of the BL as found by the LES model and as found by both MLM. The MLM represented by the solid red line is the model in which surface fluxes, entrainment rate and precipitation (maximum value and surface value) are prescribed. This line is very close to the LES result during the first 18 hours of the simulation. After this time, the results start to diverge meaning that the mixed-layer assumption fails. The cloud layer starts to dry faster than is expected using the MLM, resulting in less liquid water and thus in a lower LWP. The liquid water as a function of time can be found in figure 5.9.
This figure shows some interesting features. Roughly the same behaviour is found as in figure 5.8, although differences are larger. Where the first figure shows very good agreement up to 18:00 UTC, here the models diverge around 16:00 UTC. A diurnal cycle of the LWP, due to the warming of the cloud layer caused by absorption of shortwave radiation, is clearly observed in all models. It is, however, strongest in the LES model, which is a sign that the BL is more decoupled during the day than it is during the night. Around the afternoon, the difference starts to decrease again, which shows the temporary nature of decoupling caused by solar radiation. In both of the discussed figures, timing is interesting. The fact that the results really start to diverge late in the afternoon, shows that decoupling is really of the deepening-warming kind.

5.3.2 MLM independent of LES results

The picture sketched by the discussion above is promising. When the actual entrainment rate is used, the MLM predicts the cloud top and cloud base height extremely well for the first 16 hours. A good stand-alone MLM is therefore certainly possible. Figures 5.8 and 5.9 contain results of such a MLM, which shows that a lot of work must still be done. Many of the differences observed are caused by the parametrized entrainment,

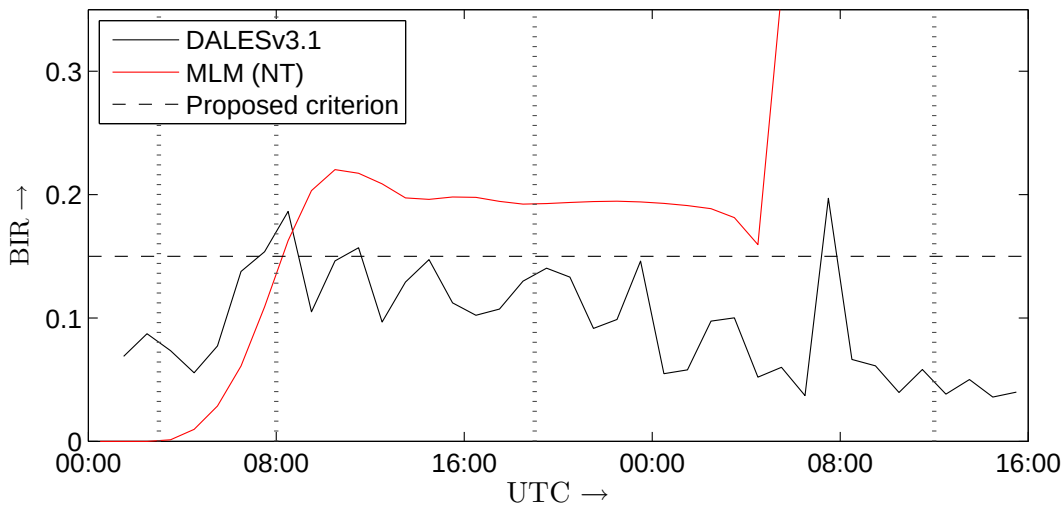

Figure 5.7: The hourly averaged BIR values plotted as a function of time as found by DALES (solid black line) and as found by the stand-alone MLM model (red line) with the decoupling criterion as suggested by Bretherton and Wyant (1997) (horizontal dashed line). The vertical dotted lines represent the average flight hours for flights 2 - 5.

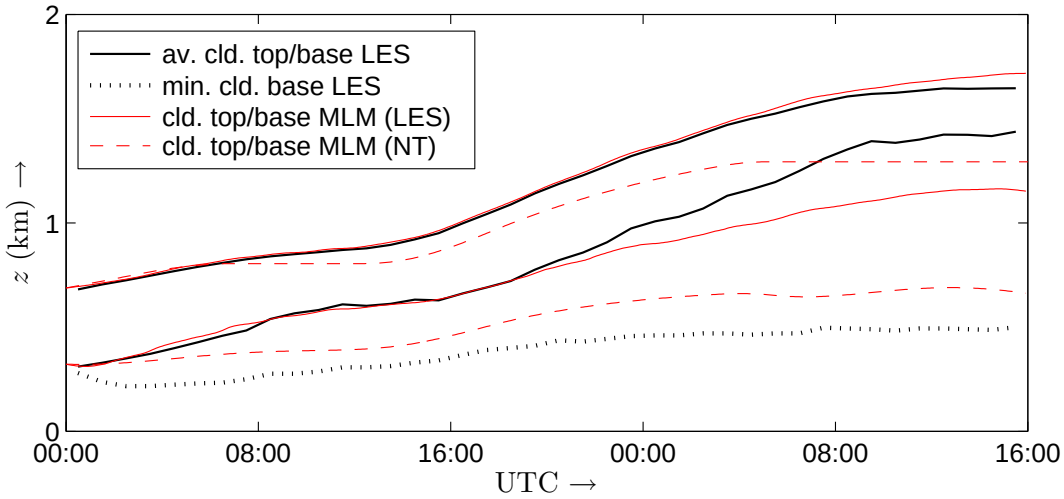

Figure 5.8: The BL evolution as found by DALES (black lines, solid and dotted as before) as well as the cloud top and cloud bottom height as found by the MLM. One case uses the entrainment, surface fluxes and precipitation as diagnosed by the LES model (solid red) while for the other case is completely independent of the LES model (dashed red).

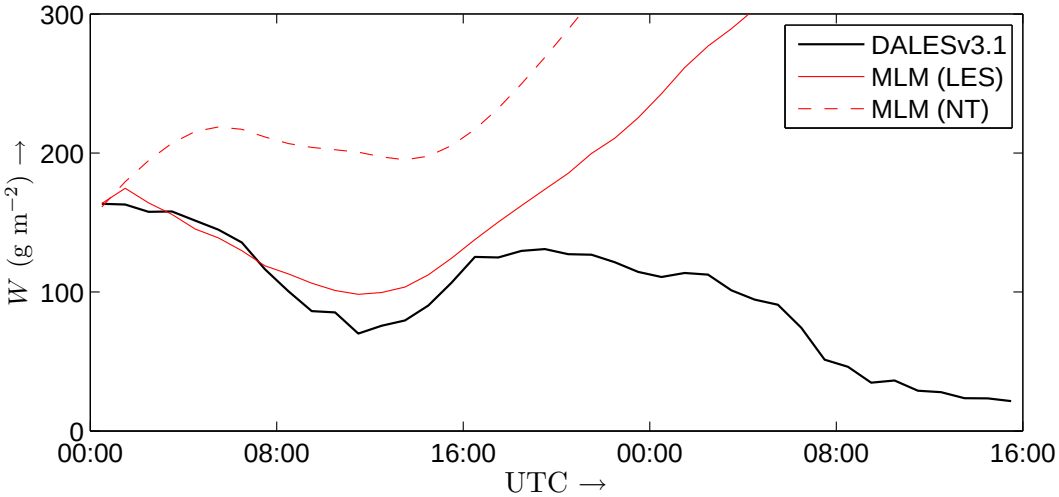

Figure 5.9: The hourly averaged liquid water path as a function of time as found by DALESv3.1 (solid black line), the MLM with prescribed LES parameters (red solid line) and by the stand-alone MLM (red dashed line). A clear diurnal cycle is observed, with minima around 12:00 UTC.

shown in figure 5.10.
During the nights, in the absence of shortwave radiation, the parametrized entrainment seems to be quite good. At daytime however, the entrainment rate is severely underestimated, leading to the lower cloud top in figure 5.8. As was noted in the MLM description, the entire contribution of shortwave radiation was included at the top of the BL, as is also done for the effects of longwave cooling and precipitation. Apparently, this leads to wrong buoyancy profiles, causing a wrong parametrization of the entrainment rate.
Less entrainment means also less dilution of the BL by the warmer and dryer FA air. The more humid and cooler BL leads to a lower cloud base and therefore a higher LWP.

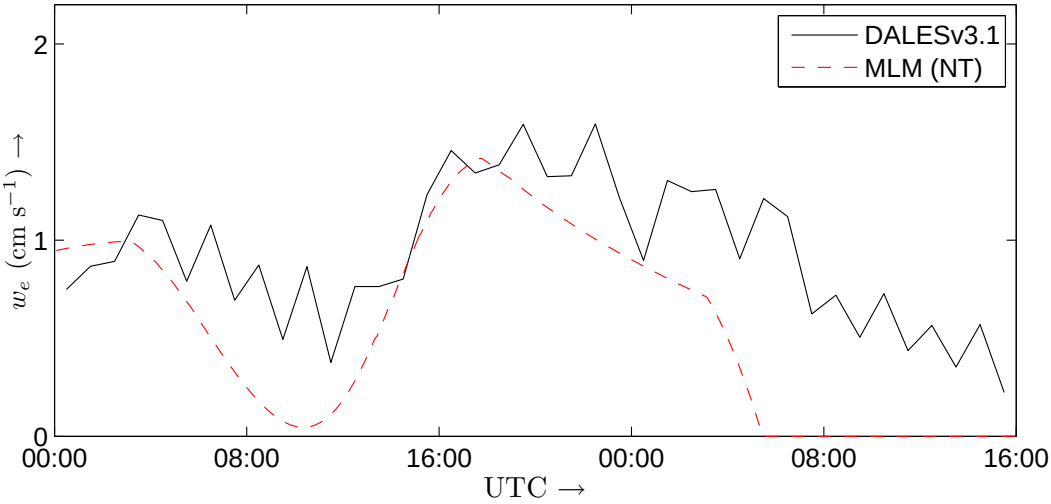

Figure 5.10: The hourly averaged entrainment rate as diagnosed by DALESv3.1 (solid black line) and as parametrized in the MLM by the NT parametrization, with $a_2 = 30$ (dashed red line).

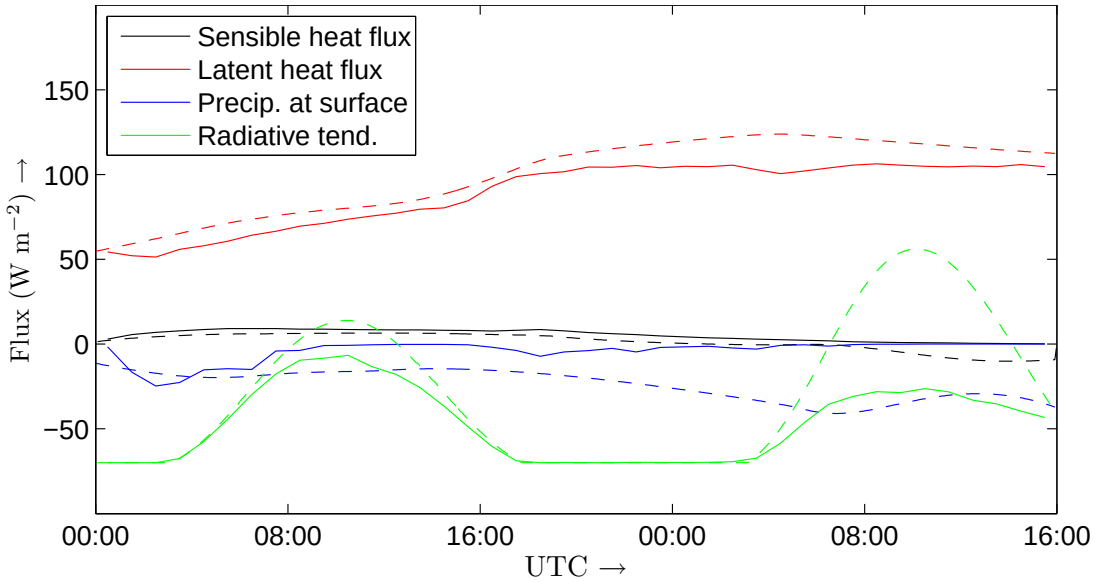

Figure 5.11: A plot of the different fluxes that are of influence on the development of the BL: the sensible heat flux $\overline{w'\theta_l'}$ and the latent heat flux $\overline{w'q_t'}$ at the surface (respectively in black and red), the precipitation flux at the surface (blue) and the total radiative flux DF_R in the BL (in green). The solid lines give hour averaged LES results, while the dashed lines represent the MLM results.

The effect is a less strong diurnal cycle in the LWP, which is also observed in figure 5.9. During the first day, in which the mixed-layer assumption is valid, the LWP is overestimated by a factor of two.

The inconsistent LWP has two clear effects, namely: the overestimation of absorption of shortwave radiation and too high precipitation rates. Both effects are clear in the plot shown in figure 5.11. During the first day, the radiative effect from the sun is strong enough to compensate entirely for radiative cooling, while during the second day the

effect has worsened. The same picture is shown by the precipitation rate: initially this rate is quite good, perhaps also due to high values predicted by the LES model. Further into the simulation, precipitation as found by the MLM keeps increasing, while it becomes virtually zero in DALES.
The surface fluxes given by equations (2.82) and (2.83) are, in contrast to the discussion above, quite close to those in the LES model. In the parametrization, $|\vec{U}|$, the velocity at 10 meters height, was decreased to 7 m s^{-1}, which is slightly lower than the approximately 10 m s^{-1} geostrophic wind forcing in the LES model. This was done to compensate for the effect of wind shear at 10 meters height.
A last question is whether or not the MLM can be used to predict decoupling of the BL. The value of BIR shown in figure 5.7 suggests it can. The values found by the MLM are in general quite high, even with the large underestimation of cloud base height, but roughly the shape is comparable to that found by DALES. A decoupling criterion based on the BIR value can therefore also be used in the MLM.

Chapter 6

Conclusions and outlook

After discussing the results, conclusions can be drawn regarding the performance of the DALESv3.1 and the usability of the MLM in predicting cloud break-up in general and decoupling in particular. This will be the topic of the first section of this chapter. The other section contains recommendations based on the research presented in this thesis.

6.1 Conclusions

6.1.1 Model intercomparison

(*i*) *Changes made in DALES during the last decade, have had a great impact on model results of STBLs.* Using the existing model intercomparison cases based on ASTEX, the entrainment rate of the most recent version of DALES was shown to be much smaller than that in the older model used by Cuijpers. This is desirable, as the old version was not capable of realistically representing the STBL as observed during DYCOMS II (Stevens et al., 2005), due to too large entrainment rates.

(*ii*) *While the precipitation rate in STBLs is usually small, it is very important for the turbulence structure of the BL.* In the process of rain drop formation, cloud water is removed, especially from the top of the boundary layer since the liquid water content is highest there. The turbulent flux of moisture, which does not include rain water, therefore increases strongly inside the cloud layer. Furthermore, the evaporation of rain water below cloud base leads to cooling of the subcloud layer. The result is a stronger decoupled BL than would be expected when microphysical effects are neglected.

6.1.2 Transition as simulation by DALES

(*iii*) *The DALES model is capable of simulating a Sc to Cu transition, like that observed during ASTEX.* The whole trajectory from a well-mixed Sc layer towards a deeper, decoupled BL, containing Cu cloud structures is well-represented by the simulation. The mean state results are very close to observations made during the first Lagrangian of ASTEX and the increase of the buoyancy flux between the third and the fourth flight is also very well represented. The vertical velocity variance, however, is too low during the first 8 hours, possibly due to the slightly to low surface flux of heat and the overestimated humidity flux.

(*iv*) *A positive, nonzero value of BIR is not a measure for the instantaneous decoupling of the BL, but it shows the tendency of a BL toward decoupling.* A positive, nonzero BIR value indicates negative buoyancy fluxes below cloud base. The profile of the vertical velocity variance is, however, not instantly affected by this. The simulation of the Sc to Cu transition indicates that persisting BIR values > 0 will eventually lead to decoupling, as was suggested by Stevens (2000). A criterion based on BIR should not be based on a critical value but on its cumulative effect.

(*v*) *The mechanism causing cloud thinning and eventually the cloud break-up of the Sc layer is deepening-warming decoupling.* Signs of CTEI, i.e. a strong increase in entrainment rate, have not been found in the simulation. The combination of the LES results with the MLM shows that when decoupling has set in (after about 16 hours), the cloud layer thins even during the night, because the moisture flux from the surface to the cloud layer is partly cut off, and cloud break-up follows. The observed formation of Cu clouds below the Sc layer is also inherent to decoupling.

6.1.3 Mixed-Layer Modeling of the transition

(*vi*) *The mixed-layer assumption is valid during the first part of the transition, but fails during the second night, due to the strong effect of BL decoupling.* A MLM with prescribed entrainment rate, surface fluxes and precipitation as calculated from the LES, describes the BL very well during the first 16 hours of the simulation, showing that the BL is well-mixed. In the remainder of the MLM simulation, cloud thickness is overestimated, resulting in a much too large LWP compared to the LES results. The reason is that the BL in the LES results is decoupled, which causes drying of the cloud layer, while the subcloud layer moistens. The MLM cannot simulate this effect.

(*vii*) *The effects of precipitation and longwave radiative cooling on the parametrized entrainment in the MLM, are well represented, which is not the case for the effect of absorption of shortwave radiation.* The entrainment parametrization of NT performs very well when longwave radiative cooling and precipitation are included at the BL top. When including the shortwave radiative flux in a similar way, entrainment rates are severely underestimated. A more realistic way of implementing shortwave radiation has to be developed.

6.2 Outlook

Recommendations based on the research presented in this thesis can be divided into two topics: 1) the use of DALES or LES models in general and possible improvements in it and 2) the use of the MLM.

6.2.1 Analysis using DALES

The simulation of the BL using the most recent version of DALES has proved successful. Still, there are points of improvement. It would, for instance, be interesting, to prescribe the geostrophic wind more accurately, instead of using a constant value for the velocity. The measurements show that it decreases rapidly in the second part of the simulation,

to a value of only 3.5 m s^{-1} during the last flight. The influence of this change on the surface fluxes of q_t and θ_l must be significant.
In the first part of the simulation however, differences between simulated and measured surface fluxes of heat and moisture are already found, even though the prescribed velocity of the geostrophic wind is accurate. More research is therefore needed. A series of simulations using DALES, for instance based on one of the existing intercomparison cases, in which a prescribed SST is used, could be used to get more insight in the dependence of the surface fluxes of heat and moisture on the BL temperature and the humidity content. Slightly varying the initial (BL) values of these variables, results in differences in the surface fluxes, making a sensitivity analysis possible. Such an experiment will also show how strong the influence of these fluxes is on the vertical profile of the vertical velocity variance and whether or not the observed differences, between DALES results and measurements during the transition, can be fully ascribed to the differences found in the surface fluxes of q_t and θ_l.
The simulation of the transition as it is presented in this thesis is the basis of the newest GCSS model intercomparison case, although some changes have been made, for instance with respect to the mentioned geostrophic wind forcing, as well as the radiative forcing of the FA. Furthermore, the surface fluxes are parametrized in this intercomparison case, which makes the analysis of differences between models in, for instance, the entrainment rate easier. In particular, the influence of precipitation and (shortwave) radiation on the entrainment rate is important. Including these schemes in LES models is relatively new. A large model intercomparison can give more insight in how these processes influence the entrainment rate and how entrainment parametrizations can be adjusted to include these effects.

6.2.2 Possibilities of the MLM

The MLM has shown great potential in the comparisons with the results of DALES presented in this thesis. It is clear that it predicts STBLs almost perfectly, as long as the degree of decoupling is not too high. Furthermore, decoupling can be diagnosed to a certain extent in the MLM, which gives the model itself the possibility to determine whether or not it may be used in a specific situation.
Since several days can be simulated in only a few seconds, sensitivity experiments can be performed, in which the influence of different parameters on the time of the onset of decoupling, is examined. These parameters may, for instance, include the SST (or the rate of SST increase during a transition), the subsidence rate, the jumps of q_t and θ_l over the inversion, the initial inversion height etc. In the line of deepening-warming decoupling, it could for instance be interesting to do a thousand or so simulations with slightly different inversion heights and/or varying latent heat fluxes. A higher inversion height or latent heat flux is expected to lead to decoupling sooner than a lower one. Bretherton and Wyant (1997) suggest, as a rule of thumb, that a latent heat flux of 100 W m^{-2} indicates a decoupled BL. Using the MLM, suggestion can be easily examined for different boundary layer heights.
An improvement of the MLM is still required in the way absorption of solar radiation is modeled, since including the entire shortwave radiative flux at the top of the BL was shown to lead to bad values of the parametrized entrainment. This improvement will be achieved by making the effect of warming by absorption of shortwave radiation in the cloud layer, a function of height. In contrast to longwave radiative cooling, which

takes place in the top 40 meters of the cloud, shortwave radiation absorption takes place throughout the entire cloud layer. Since the net profile of shortwave radiation is already calculated, it is fairly easy to make the source term height dependent. Of course, this has no effect on the total forcing, but the buoyancy flux profile *is* affected. Since the parametrization of NT is highly dependent on this profile, the parametrized entrainment rate changes, possibly matching the LES results better. In a similar way, the representation of precipitation in the vertical profiles of the turbulent moisture and heat fluxes can be improved by making the sink/source term dependent of height.
In this thesis, the MLM was used in two forms: a version in which the surface fluxes of heat and moisture, the entrainment rate and the precipitation where prescribed and a version in which all of these effects are parametrized. However, any intermediate form is possible, for instance a version in which entrainment from the LES model results is used (perhaps because the MLM produces large errors), while precipitation and surface fluxes are parametrized. By, example given, varying the SST, the influence of the surface fluxes on the evolution of the mean state of the BL, on the precipitation rate and eventually on the decoupling of the BL can be examined.
No MLM, however, will predict the thinning of the BL due to decoupling. It would therefore be interesting to switch from a MLM to a two-layer model, as described in Smith and Jonas (1995), when the BL is decoupled. In such a model, the dynamics of the upper layer are dominated by Cu clouds. A criterion based on the value of BIR, can be used to switch between the models. Ultimately, it might be possible to describe the entire transition from a STBL to a Cu-topped BL, using these relatively simple models.

Bibliography

B.A. Albrecht and R.S. Penc. An observational study of cloud-topped mixed layers. *Journal of the Atmospheric Sciences*, 42:800–822, 1985.

B.A. Albrecht, D.A. Randall, and S. Nicholls. Observations of marine stratocumulus clouds during FIRE. *Bulletin of the American Meteorological Society*, 69:618–626, 1988.

B.A. Albrecht, C.S. Bretherton, D. Johnson, W.H. Scubert, and A.S. Frisch. The atlantic stratocumulus transition experiment - ASTEX. *Bulletin of the American Meteorological Society*, 76:889–904, 1995.

D.A. Bennetts, E. McCallum, S. Nicholls, and J.R. Grant. Stratocumulus: an introductory account. *The Meteorological Magazine*, 115:65–76, 1986.

A.K. Betts. Non-precipitating cumulus convection and its parameterization. *The Quarterly Journal of the Royal Meteorological Society*, 99:178–196, 1973.

E. Boeker and R. van Grondelle. *Environmental Physics*. John Wiley and Sons, 1999.

C. S. Bretherton and M.C. Wyant. Moisture transport, lower-tropospheric stability, and decoupling of cloud-topped boundary layers. *Journal of the Atmospheric Sciences*, 54: 148–167, 1997.

C.S. Bretherton and R. Pincus. Cloudiness and marine boundary layer dynamics in the ASTEX lagrangian experiments. Part I: Synoptic setting and vertical structure. *Journal of the Atmospheric Sciences*, 52:2707–2723, 1995.

C.S. Bretherton, S.K. Krueger, M.C. Wyant, P. Bechtold, E. van Meijgaard, B. Stevens, and J. Teixeira. A GCSS boundary-layer cloud model intercomparison study of the first ASTEX lagrangian experiment. *Boundary-Layer Meteorology*, 93:341–380, 1999.

P. Caldwell and C.S. Bretherton. Response of a subtropical stratocumulus-capped mixed layer to climate and aerosol changes. *Journal of Climate*, 22:20–38, 2009.

P.E. Ciesielski, W.H. Schubert, and R.H. Johnson. Large-scale heat and moisture budgets over the ASTEX region. *Journal of the Atmospheric Sciences*, 56:3241–3261, 1999.

K. Comstock, R. Wood, S.E. Yuter, and C.S. Bretherton. Reflectivity and rain rate in and below drizzling stratocumulus. *The Quarterly Journal of the Royal Meteorological Society*, 130:2891–2918, 2004.

J.W.M. Cuijpers. *Large-Eddy Simulation of Cumulus Convection*. PhD thesis, Delft - University of Technology, 1994.

J.W.M. Cuijpers and P.G. Duynkerke. Large-Eddy Simulation of trade-wind cumulus clouds. *Journal of the Atmospheric Sciences*, 50:3894–3908, 1993.

S.R. de Roode. *Cloudy boundary layers. Observations and mass-flux parameterizations.* PhD thesis, University of Utrecht, 1999.

S.R. de Roode. *Clouds.* University of Utrecht, 2004.

S.R. de Roode and P.G. Duynkerke. Observed lagrangian transition of stratocumulus into cumulus during ASTEX: mean state and turbulent structure. *Journal of the Atmospheric Sciences*, 54:2157–2173, 1997.

J.W. Deardorff. *Three-dimensional modeling of the planetary boundary layer.* American Meteorological Society, 1973. Workshop on Meteorology.

J.W. Deardorff. Usefulness of liquid-water potential temperature in a shallow-cloud model. *Journal of Applied Meteorology - Notes and Correspondence*, 15:98–102, 1976.

P.G. Duynkerke, H. Zhang, and P.J. Jonker. Microphysical and turbulent structure of nocturnal stratocumulus as observed during ASTEX. *Journal of the Atmospheric Sciences*, 52:2763–2777, 1995.

P.G. Duynkerke, P.J. Jonker, A. Chlond, M.C. van Zanten, J. Cuxart, P. Clark, E. Sanchez, G. Martin, G. Lenderink, and J. Teixeira. Intercomparison of three- and one-dimensional model simulations and aircraft observations of stratocumulus. *Boundary-Layer Meteorology*, 92:453–487, 1999.

P.G. Duynkerke, S.R. de Roode, M.C. van Zanten, J. Calvo, J. Cuxart, S. Cheinet, A. Chlond, H. Grenier, P.J. Jonker, M. Khler, G. Lenderink, D. Lewellen, C. Lappen, A.P. Lock, C. Moeng, F. Mller, D. Olmeda, J. Piriou, E. Sanchez, and I. Sednev. Observations and numerical simulations of the diurnal cycle of the EUROCS stratocumulus case. *The Quarterly Journal of the Royal Meteorological Society*, 130:3269–3296, 2004.

Y. Fouquart and B. Bonnel. Computations of solar heating of the Earth's atmosphere: A new parametrization. *Beitraege zur Physik der Atmosphaere*, 53:35–62, 1980.

T Heus. *On the edge of a cloud.* PhD thesis, TUDelft, 2008.

T Heus, C.C. van Heerwaarden, H.J.J. Jonker, A.P. Siebesma, S. Axelsen, O. Geoffroy, A. Moene, D. Pino, S.R. de Roode, and J. Vila-Guerau de Arellano. An overview of the Dutch Atmospheric LES. *Geoscientific Model Development*, in preperation, 2009.

J.T. Houghton, L.G.M. Filho, D.J. Griggs, and K. Maskell. An introduction to simple climate models used in the IPCC second assessment report. Technical report, Intergovernmental Panel on Climate Change, 1997.

M. Khairoutdinov and Y. Kogan. A new cloud physics parametrization in a Large-Eddy Simulation model of marine stratocumulus. *Monthly Weather Review*, 128:229–243, 2000.

H.-C. Kuo and W.H. Schubert. Stability of cloud-topped boundary layers. *The Quarterly Journal of the Royal Meteorological Society*, 114:887–916, 1988.

M. Lesieur, O. Metais, and P. Comte. *Large-Eddy Simulations of Turbulence*. Cambridge University Press, 2005.

D.K. Lilly. Models of cloud-topped mixed layers under a strong inversion. *The Quarterly Journal of the Royal Meteorological Society*, 94:292–309, 1968.

C.-H. Moeng. Entrainment rate, cloud fraction and liquid water path of planetary boundary layer stratocumulus clouds. *Journal of the Atmospheric Sciences*, 57:3627–3643, 2000.

M.J. Moran and H.N. Shapiro. *Fundamentals of Engineering Thermodynamics*. John Wiley and Sons, 2002.

S. Nicholls. The dynamics of stratocumulus: aircraft observations and comparisons with a mixed layer model. *The Quarterly Journal of the Royal Meteorological Society*, 110: 783–820, 1984.

S.B. Pope. *Turbulent Flows*. Cambridge University Press, 2005.

B.W. Rossow and R.A. Schiffer. Advances in understanding clouds from ISCCP. *Bulletin of the American Meteorological Society*, 80:2261–2287, 1999.

A. Seifert and K.D. Beheng. A double-moment parameterization for simulating autoconversion, accretion and selfcollection. *Atmospheric Research*, 59-60:265–281, 2001.

S.A. Smith and P.R. Jonas. A diagnostic model of turbulent transport in a cumulus cloud layer. *Atmospheric Research*, 39:127–143, 1995.

B. Stevens. Cloud transitions and decoupling in shear-free stratocumulus-topped boundary layers. *Geophysical Research Letters*, 27:2557–2560, 2000.

B. Stevens. Entrainment in stratocumulus topped mixed layers. *The Quarterly Journal of the Royal Meteorological Society*, 128:2663–2690, 2002.

B. Stevens, D.H. Lenschow, I. Faloona, C.H. Moeng, D.K. Lilly, B. Blomquist, G. Vali, A. Bandy, T. Campos, H. Gerber, S. Haimov, B. Morley, and D. Thornton. On entrainment rates in nocturnal marine stratocumulus. *The Quarterly Journal of the Royal Meteorological Society*, 129:3469–3493, 2003a.

B. Stevens, C.H. Moeng, A.S. Ackerman, C.S. Bretherton, A. Chlond, S. de Roode, J. Edwards, J.C. Golaz, H. Jiang, M. Khairoutdinov, M.P. Kirkpatrick, D.C. Lewellen, A. Lock, F. Mller, D.E. Stevens, E. Whelan, and P. Zhu. Evaluation of Large-Eddy Simulations via observations of nocturnal marine stratocumulus. *Monthly Weather Review*, 133:14431462, 2005.

Bjorn Stevens, Donald H. Lenschow, Gabor Vali, Hermann Gerber, A. Bandy, B. Blomquist, J.-L. Brenguier, C. S. Bretherton, F. Burnet, T. Campos, S. Chai, I. Faloona, D. Friesen, S. Haimov, K. Laursen, D. K. Lilly, S. M. Loehrer, Szymon P. Malinowski, B. Morley, M. D. Petters, D. C. Rogers, L. Russell, V. Savic-Jovcic, J. R. Snider, D. Straub, Marcin J. Szumowski, H. Takagi, D. C. Thornton, M. Tschudi, C. Twohy, M. Wetzel, and M. C. van Zanten. Dynamics and chemistry of marine stratocumulus - DYCOMS-II. *Bulletin of the American Meteorological Society*, 84(5): 579–593, 2003b.

R.B. Stull. *An Introduction to Boundary Layer Meteorology.* Kluwer Academic Publishers, 1993. Appendix D.

J.D. Turton and S. Nicholls. A study of the diurnal variation of stratocumulus using a multiple mixed layer model. *The Quarterly Journal of the Royal Meteorological Society*, 113:969–1009, 1987.

M. Van Zanten. *Entrainment processes in stratocumulus.* PhD thesis, University of Utrecht, 2000.

M.C. Wakefield and W.H. Schubert. Mixed-layer model simulation of eastern north pacific stratocumulus. *Monthly Weather Review*, 109:1952–1968, 1981.

Appendix A

List of symbols and abbreviations

The first table in this appendix, table A.3, contains an extensive list of symbols used throughout this thesis, while the second table gives an explanations of some of the most used formats in which a variable φ can be found (table A.2). Lastly, because of the multitude of abbreviations to which the reader might not be familiar with, table A.3 contains the abbreviated and complete forms of those used.

Table A.1: A list of symbols used in this thesis, starting with some frequently used subscripts. Brackets around a variable in the last column mean the units of the variable between them need to be inserted.

Subscript	Description
0	Reference state
d	Dry air value
i, j, k	1, 2 or 3; Carthesian direction
l	Liquid water
lw	Longwave (radiation)
ml	Boundary layer averaged value
s	Saturation value
sw	Shortwave (radiation)
$surf$	Value at the surface
t	Total water (vapor + liquid)
v	Water vapour (for q)/Virtual (for T and θ)
w	Saturated air value

Symbol	Name/description	Units
$\mathfrak{A}$	Efficiency of entrainment generation by turbulence	-
$\mathfrak{D}$	Represents contribution in entrainment rate due to non-turbulent processes	m s^{-1}
$\mathfrak{W}$	Work term associated with turbulent processes	K m s^{-1}
α	Kolmogorov constant	-
Δ	Gridsize	m

continued on next page

continued from previous page

δ_{ij}	Kronecker delta	-
ε	Dissipation rate of TKE	J s^{-1}
ϵ	Constant ≈ 0.622	-
ϵ_I	Constant ≈ 0.608	-
ϵ_{ijk}	Alternating unit tensor	-
η	Unit vector	-
θ	Potential temperature	K
θ_e	Equivalent potential temperature	K
λ	Lengthscale	m
μ	Dynamic viscosity	Pa s
μ	Variable related to the importance of top-down fluxes; only used in eqs. (2.95) and (2.96)	Pa s
Π	Exner function	-
π	Modified pressure	J
ρ	Density	kg m^{-3}
$\tau_j^{(\varphi)}$	Subfilter scale flux of φ	$[\varphi]$ m s^{-1}
τ_{ij}	Residual stress tensor	m^2 s^{-1}
τ_{ij}^{an}	Anisotropic residual stress tensor	m^2 s^{-1}
φ	Variable	-
ϕ	Latitude	rad
ω	Earth's angular velocity	rad s^{-1}
A	Coefficient	kg kg^{-1}
A_NT	Parameter in the entrainment parametrization of NT	-
a_2	Coefficient	-
B	Coefficient	K
b_m	Coefficient	m^2 kg^{-1}
C_D	Exchange coefficient	-
c_f	Filtering coefficient	-
$c_{m,h,\varepsilon,N}$	Subfilter scale coefficients (see table 2.2)	-
c_p	Specific heat at constant pressure	J kg^{-1} K^{-1}
D	Divergence of air in horizontal directions	s^{-1}
e	Turbulent kinetic energy	J
F	External body force	N m^{-3}
F_R	Net radiative flux	K m s^{-1}
F_p	Precipitation flux	kg s^{-1} m^{-2}
F^c	Coriolis body force	N m^{-3}
F^g	Gravitational body force	N m^{-3}
G	Normalized filter function	-
g	Gravitational acceleration	m s^{-2}
h	Specific enthalpy	J kg^{-1}

continued on next page

continued from previous page

K_h	Diffusivity constant for q_t and θ_l	$m^2\ s^{-1}$
K_m	Diffusivity constant for velocity	$m^2\ s^{-1}$
k	Absorption coefficient	$m^2\ kg^{-1}$
k_f	Filter wavenumber	m^{-1}
k_p	Constant	$\mu m^{3.75}\ m^{-1.5}$
L	Latent heat of evaporation of water	$J\ kg^{-1}$
N_c	Droplet number concentration	cm^{-3}
p	Pressure	Pa
q	Water content	$kg\ kg^{-1}$
q_i	Water content in the ice (solid) phase	$kg\ kg^{-1}$
r	Integration variable, position	m
Ri	Richardson number	-
R_m	Specific gas constant of a mixture of gases	$J\ kg^{-1}\ K^{-1}$
$\overline{r}$	Mean radius of truncated exponential distr. at cloud base	m
S_φ	Total of source/sink terms for variable phi	$[\varphi]\ s^{-1}$
S_φ^R	Source/sink term for variable phi due to radiation	$[\varphi]\ s^{-1}$
S_φ^P	Source/sink term for variable phi due to precipitation	$[\varphi]\ s^{-1}$
s_l	Liquid water static energy	$J\ kg^{-1}$
s	Specific enthalpy	$J\ kg^{-1}\ K^{-1}$
T	Temperature	K
$T_j^{(\varphi)}$	Flux of φ due to deviations from the average	$[\varphi]\ m\ s^{-1}$
t	Time	s
U	Velocity at 10 meters height relative to the surface	$m\ s^{-1}$
u_*	Friction velocity	$m\ s^{-1}$
$\{u_1, u_2, u_3\}$	Velocity in x-, y- and z-direction	$m\ s^{-1}$
$\{u, v, w\}$	Velocity in x-, y- and z-direction	$m\ s^{-1}$
u_g, v_g	Geostrophic wind velocity in x- and y-direction	$m\ s^{-1}$
$\{x, y, z\}$	Carthesian coordinates	m
W	Liquid Water Path	$kg\ m^{-2}$
w^*	Convective velocity scale	$m\ s^{-1}$
w_e	Entrainment velocity	$m\ s^{-1}$
z_0	Surface roughness	m
z_b	Cloud base height	m
z_i	Inversion height	m
z_t	Cloud top height	m

Table A.2: Explanation of some frequently used 'operators' on variables φ.

$\widetilde{\varphi}$	Filtered part
φ''	Subfilter scale part
$\overline{\varphi}$	Reynolds-averaged part
φ'	Deviation from Reynolds average
$\overline{w'\varphi'}$	Turbulent flux, or: flux of φ due to deviations from the average
$\varphi\big\vert_z$	Value of φ at height z
$\vec{\varphi}$	The vector φ
$\Delta\varphi$	Change of φ over the inversion

Table A.3: A list of all abbreviations used in this thesis with their complete form.

lhs	left-hand side
rhs	right-hand side
ABL	Atmospheric Boundary Layer
ASTEX	Atlantic Stratocumulus Transition EXperiment
BIR	Buoyancy Integral Ratio (pp. 42)
BL	Boundary Layer
CCN	Cloud Condensation Nuclei
CM	The entrainment parametrization of Moeng (2000)
CTEI	Cloud Top Entrainment Instability
Cu	Cumulus
DALES	Dutch Atmospheric Large Eddy Simulation
DNS	Direct Numerical Simulation
DYCOMS	DYnamics and Chemistry Of Marine Stratocumulus
ECMWF	European Centre for Medium-Range Weather Forecasts
EUCREM	EUropean Cloud REsolving Modelling
EUMETSAT	EUropean organisation for the exploitation of METeorological SATellites
ISCCP	International Satellite Cloud Climatology Project
FA	Free Atmosphere
FFT	Fast Fourier Transform
FIRE	First ISCCP Regional Experiment
GCSS	GEWEX Cloud System Study
GEWEX	Global Energy and Water Cycle Experiment
KK	The bulk microphysics scheme of Khairoutdinov and Kogan (2000)
LES	Large Eddy Simulation
LWP	Liquid Water Path
NT	The entrainment parametrization of Turton and Nicholls (1987)
Sc	Stratocumulus
SCM	Single Column Model
SFS	Subfilter scale
SGS	Subgrid scale
SST	Sea Surface Temperature
STBL	Stratocumulus-Topped Boundary Layer
TKE	Turbulent Kinetic Energy
UTC	Coordinated Universal Time